

AD-A115 474 COLORADO STATE UNIV FORT COLLINS DEPT OF CHEMISTRY

F/G 20/R

USF6 ENERGY LEVELS AND VIBRONIC COUPLING IN THE (DT2G)2 CONFIGU--ETC(U)

UNCLASSIFIED

TR-6

N00014-79-C-0647

NL

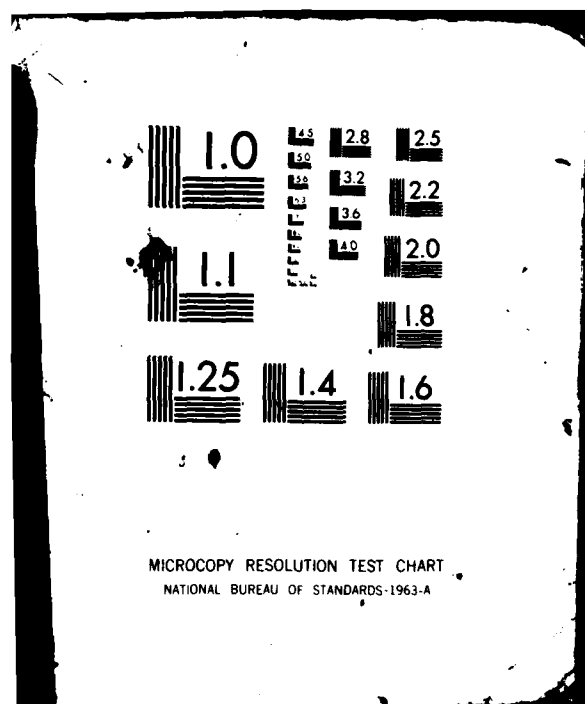
$$\frac{1}{2} \left( \frac{1}{2} + \frac{1}{2} \right) = \frac{1}{2}$$

END

DATE

7 82

DTIC



AD A115474

12

OFFICE OF NAVAL RESEARCH  
Contract N00014-79-C-0647

Technical Report No. 6

$\text{OsF}_6$  ENERGY LEVELS AND VIBRONIC COUPLING  
in the  $(d_{t_{2g}})^2$  CONFIGURATION

by

D.L. Michalopoulos and E.R. Bernstein

Prepared for Publication in  
Molecular Physics

Department of Chemistry  
Colorado State University  
Fort Collins, Colorado 80523

2 February 1981

DTIC  
ELECTE  
S JUN 11 1982 D  
E

Reproduction in whole or in part is permitted for  
any purpose of the United States Government

Approved for Public Release; Distribution Unlimited

82 06 11 024

DTIC FILE COPY

Unclassified

SECURITY CLASSIFICATION OF THIS PAGE (When Data Entered)

REPORT DOCUMENTATION PAGE		READ INSTRUCTIONS BEFORE COMPLETING FORM
1. REPORT NUMBER Technical Report #6	2. GOVT ACCESSION NO. AD-A115474	3. RECIPIENT'S CATALOG NUMBER
4. TITLE (and Subtitle) OsF <sub>6</sub> Energy Levels and Vibronic Coupling in the (d <sub>t2g</sub> ) <sup>2</sup> Configuration		5. TYPE OF REPORT & PERIOD COVERED Technical Report
7. AUTHOR(s) D.L. Michalopoulos and E.R. Bernstein		6. PERFORMING ORG. REPORT NUMBER
9. PERFORMING ORGANIZATION NAME AND ADDRESS Department of Chemistry Colorado State University Fort Collins, Colorado 80523		8. CONTRACT OR GRANT NUMBER(s) N00014-79-C-0647
11. CONTROLLING OFFICE NAME AND ADDRESS Office of Naval Research Arlington, VA 22217		10. PROGRAM ELEMENT, PROJECT, TASK AREA & WORK UNIT NUMBERS
14. MONITORING AGENCY NAME & ADDRESS (if different from Controlling Office)		12. REPORT DATE May 26, 1982
		13. NUMBER OF PAGES 51
		15. SECURITY CLASS. (of this report)
		15a. DECLASSIFICATION DOWNGRADING SCHEDULE
16. DISTRIBUTION STATEMENT (of this Report) Approved for Public Release; Distribution Unlimited		
17. DISTRIBUTION STATEMENT (of the abstract entered in Block 20, if different from Report)		
18. SUPPLEMENTARY NOTES		
19. KEY WORDS (Continue on reverse side if necessary and identify by block number) Jahn Teller Effect, Franck-Condon analysis, absorption spectra, Raman scattering, two-particle transitions, hexafluoride metals		
20. ABSTRACT (Continue on reverse side if necessary and identify by block number) Electronic and vibronic energy levels of the (d <sub>t2g</sub> ) <sup>2</sup> configuration of OsF <sub>6</sub> are studied using electronic Raman scattering and absorption spectroscopy. The ground state has been identified as E <sub>g</sub> (crystal field split by ~28 cm <sup>-1</sup> ) and the first excited state is T <sub>1g</sub> with crystal field energy levels at 14, 28 and 40 cm <sup>-1</sup> . The three other regions of the spectrum that have been observed are at 4,000 cm <sup>-1</sup> , 8,000 cm <sup>-1</sup> , and 17,000 cm <sup>-1</sup> covering the remaining (d <sub>t2g</sub> ) <sup>2</sup> configuration levels. The 4,000 cm <sup>-1</sup> band consists of A <sub>1g</sub> and T <sub>1g</sub> electron states which do not interact strongly through vibronic coupling. The T <sub>1g</sub> electronic state evidences a strong		

Unclassified

SECURITY CLASSIFICATION OF THIS PAGE(When Data Entered)

20. (D 2.2) linear Jahn Teller effect for  $\nu_5$  and an observable Jahn Teller effect for  $\nu_2$ . The band at  $8,000 \text{ cm}^{-1}$  consists of  $E_g$  and  $T_{2g}$  electronic states; it is so complex and strongly coupled that little information can be extracted from the absorption data concerning the Jahn-Teller interaction in this 5-fold degenerate manifold. The feature at  $17,000 \text{ cm}^{-1}$  is an  $A_{1g}$  electronic state and its elucidation follows normal behavior found in other hexafluoride spectra.

Accession For	
NTIS GRA&I	<input checked="checked" type="checkbox"/>
DTIC TAB	<input type="checkbox"/>
Unannounced	<input type="checkbox"/>
Justification	
By	
Distribution/	
Availability Codes	
Avail and/or	
Dist	Special
A	



## I. INTRODUCTION

Metal hexafluorides have been the objects of much study, both theoretical and experimental, in the last two decades. Two areas of particular interest have been the electronic spectra and structure of these molecules, and vibronic coupling. These interests have been sparked by the physical nature of the systems: low-lying electronic states with sharp assignable features, high molecular symmetry ( $O_h$ ) resulting in electronic and vibrational degeneracies, and few vibrations (six) which obey known systematics.

Previous work with  $OsF_6$  entailed a ground state vibrational analysis using absorption and Raman scattering data of gaseous and liquid samples.<sup>1</sup> These ground state frequencies are shown in Table I. The broad nature of  $\nu_2(e_g)$  bands was interpreted as being the result of an  $E_g \otimes e_g$  Jahn-Teller Effect (JTE).

Moffitt et al. obtained absorption spectra in the region between 4,000 and 50,000  $cm^{-1}$  for gaseous  $OsF_6$ .<sup>2</sup> Three distinct types of band systems were observed. The first, found between 4,000 and 18,000  $cm^{-1}$ , consists of three separate bands with irregular, well resolved vibrational patterns. Each of these three bands has an overall width on the order of 1,000  $cm^{-1}$ . The second kind, between 35,000 and 40,000  $cm^{-1}$ , with band widths of several thousand wavenumbers and little or no structure, are superimposed on a very intense continuum beginning at 22,500 and extending past 50,000  $cm^{-1}$ . This continuum, the third band type, was assigned to states originating from the transfer of charge from the fluorine ligands to the central metal atom, while the first two were assigned as originating from the  $(d_{t_{2g}})^2$  and  $(d_{t_{2g}})^1(d_{e_g})^1$  electron configura-

rations, respectively. It is this first type of state, i.e., the  $(d_{t_{2g}})^2$  ligand field states, which we report on in this paper.

As mentioned above, the hexafluorides possess electronic and vibrational degeneracy. They are expected, therefore, to evidence strong vibronic coupling. Recent work involving the  $\Gamma_8$  electronic states of  $\text{IrF}_6$ <sup>3,4,5,6</sup> and  $\text{ReF}_6$ <sup>7</sup> have shown that standard linear Jahn-Teller (LJT) theory proves inadequate in describing the  $\Gamma_8 \otimes e_g$  and  $\Gamma_8 \otimes t_{2g}$  interactions. A coupling scheme including quadratic terms in the JT Hamiltonian and simultaneous treatment of both active vibrational modes was needed to explain spectral features.

A Franck-Condon analysis<sup>8</sup> of  $\nu_5(t_{2g})$  progressions in the emission spectrum from the first charge transfer band of  $\text{UF}_6$  ( $T_{1g}$  symmetry) has indicated a dominant  $T_{1g} \otimes t_{2g}$  linear Jahn-Teller Effect (LJTE). We have found direct evidence from absorption data of a dominant  $T_{1g} \otimes t_{2g}$  LJTE in the  $4,000 \text{ cm}^{-1}$   $T_{1g}$  electronic state of  $\text{OsF}_6$ .

## II. SUMMARY OF ELECTRONIC CALCULATIONS

In an effort to understand their experimental results, Moffitt and coworkers calculated the energies of the  $(d_{t_{2g}})^2$  ligand field states of  $\text{OsF}_6$ .<sup>2</sup> Assuming little or no interaction between the  $(d_{t_{2g}})^2$  and  $(d_{t_{2g}})^1(d_{e_g})^1$  configurations, or between the  $(d_{t_{2g}})^2$  configuration and charge transfer states, they were able to treat the problem as one involving an isolated manifold of  $d_{t_{2g}}$  orbitals.

Moreover, due to the isomorphism between  $(d_{t_{2g}})^n$  and atomic  $p^{6-n}$  configurations, the problem further reduced to spherical symmetry. The well known solution to this calculation involves two-parameters- spin orbit coupling and electron correlation. Indeed, it was found that the  $OsF_6$  ligand field states are fit by a  $p^4$  atomic configuration with spin orbit coupling and correlation being of the same magnitude- $3,200\text{ cm}^{-1}$ .

Eisenstein<sup>9</sup>, on the other hand, has done a calculation ignoring only the charge transfer states. Following the lines of a more conventional ligand-field calculation, he included a stereospecific potential due to the fluorine ligands, spin-orbit coupling, correlation, and configuration interaction. Subsequent diagonalization of the matrices obtained using the above interactions in an octahedral basis are compared in Table II to Moffitt's results. A schematic diagram of this method is shown in Figure 1. Two things should be noted: the group-theoretical correlation between the eigenstate representations in the spherical and octahedral bases and the predicted proximity of the members of the three pairs of states in the Eisenstein approach. Of course, these nearly degenerate states can only be distinguished from each other at low temperatures and high resolution.

### III. SUMMARY OF PERTINENT JAHN-TELLER THEORY

The vibronic Hamiltonian for a  $T_1 \otimes t_2$  LJTE is given by<sup>10</sup>



$$H(q,p) = \frac{1}{2}[p_{\xi}^2 + p_{\eta}^2 + p_{\zeta}^2 + W^2(q_{\xi}^2 + q_{\eta}^2 + q_{\zeta}^2)] \frac{L_{\tau}}{\sqrt{6}} \begin{pmatrix} 0 & q_{\zeta} & q_{\eta} \\ q_{\zeta} & 0 & q_{\xi} \\ q_{\eta} & q_{\xi} & 0 \end{pmatrix}.$$

Here,  $q$  and  $p$  are the coordinate and momentum vectors of the  $t_2$  vibrational interaction. The term within the brackets is the Hamiltonian for an unperturbed three-dimensional harmonic oscillator.

Moffitt and Thorson, using second order perturbation theory, have obtained a solution for the vibronic level energies for small  $L_{\tau}$ , i.e.,  $L_{\tau} \ll h\omega^0$ , in which  $h\omega^0$  is the energy of the unperturbed vibration. For  $L_{\tau} \sim h\omega^0$ , perturbation methods fail, and a parametric calculation is required. Caner, Englman, and Toaff have done this calculation for a molecule of  $O$  symmetry in the following manner.<sup>11</sup>

Vibronic functions, spanning representations of the point group  $O$ ,  $\Gamma_v$ , with components  $\gamma_v$  are given by:

$$|\Gamma_v, \gamma_v; \Gamma_{\tau}; n, \ell, s\rangle = [\Gamma_v]^{1/2} \sum_{\rho, \gamma_{\tau}} V \begin{pmatrix} \Gamma_{\tau} & \Gamma_1 & \Gamma_v \\ \gamma_{\tau} & \rho & \gamma_v \end{pmatrix} |\Gamma_{\tau}, \gamma_{\tau}; n, \ell, s\rangle |\rho\rangle.$$

Here,  $\Gamma_{\tau}$  and  $\gamma_{\tau}$  are the representation and component of symmetry adapted vibrational functions;  $n$  and  $\ell$  are the principal and angular

momentum vibrational quantum numbers;  $s$  is an index distinguishing different vibrational functions with same  $\Gamma_\tau$ ,  $\gamma_\tau$ ,  $n$ , and  $\ell$ ; the  $y \begin{pmatrix} \Gamma_\tau & T_1 & \Gamma_v \\ \gamma_\tau & \rho & \gamma_v \end{pmatrix}$  are coupling coefficients for the point group 0 as defined by Griffith;<sup>12</sup> the  $|\rho\rangle$  are the three components of the  $T_1$  electronic state; finally,  $[\Gamma_v]$  is the degeneracy of the vibronic function. The symmetry adapted vibrational functions are linear combinations of spherical harmonics,  $Y_\ell^m$ , defined and tabulated in the literature,<sup>13</sup> transforming as representative of the point group 0. The quantum numbers  $n$  and  $\ell$  take on the values 0,1,2,... and  $n, n-2, n-4, \dots 0$  or 1 respectively.

A secular matrix is then constructed using these functions. Since the Hamiltonian is invariant under group operations, this matrix can be put immediately in block diagonal form. Each of these blocks contains functions spanning the same representation; there are five of these block matrices, of symmetry  $A_1$ ,  $A_2$ ,  $E$ ,  $T_1$  and  $T_2$ . Each matrix is then separately diagonalized; the vibronic eigenfunctions (of symmetries  $A_1$ ,  $A_2$ ,  $E$ ,  $T_1$  and  $T_2$ ) and eigenvalues are thus generated. The eigenfunctions take the form

$$|\psi_j^{\Gamma_v \gamma_v}\rangle = \sum_{\Gamma_\tau, n, m, s} A(\Gamma_v, j; \Gamma_\tau; n, m, s) |\Gamma_v, \gamma_v; \Gamma_\tau; n, m, s\rangle$$

in which  $j(=1,2,3\dots)$  labels different eigenfunctions with the same  $\Gamma_v$  and  $\gamma_v$ . The coefficients  $A$  are obtained directly from the calculation. The eigenvalues are shown, up to  $n=3$ , in Figure 2 as a

function of  $L/\sqrt{6} h\omega^\circ$ . An alternate expression for coupling size is  $D = \frac{1}{9} \frac{(L_\tau)^2}{(h\omega^\circ)^2}$ .

#### IV. EXPERIMENTAL

Experimental procedures are detailed elsewhere.<sup>14,15</sup> Briefly, appropriate molar quantities of host ( $\text{MoF}_6$  or  $\text{WF}_6$ ) and  $\text{OsF}_6$  are distilled and mixed in a monel vacuum line (ultimate pressure :  $1 \times 10^{-7}$  torr), drawn into either a quartz or pyrex cell and glass blown off. The host materials are obtained commercially;  $\text{OsF}_6$  is synthesized via direct combination of the elements at elevated temperature and pressure.<sup>16</sup> Single crystals are grown at temperatures ( $\sim -15^\circ\text{C}$ ) below the structural phase transition temperature of the host over a period of months, cooled slowly to  $77^\circ\text{K}$  and stored under liquid nitrogen until needed.

Absorption spectra, obtained at  $1.8^\circ\text{K}$ ,  $4.2^\circ\text{K}$ , and  $77^\circ\text{K}$ , are taken with sample concentrations of .5% and 1%  $\text{OsF}_6$ . A one meter monochromator with appropriate grating and filtering is used. For infrared experiments, the apparatus included a Tungsten/Iodine lamp and liquid nitrogen cooled detector, while for visible absorption spectra a high pressure Xenon lamp and cooled photomultiplier tube are used.

Raman scattering spectra are obtained at  $4.2^\circ\text{K}$  and  $77^\circ\text{K}$  with sample concentrations ranging from 5% to 25%  $\text{OsF}_6$ . The light source is one of the lines of an  $\text{Ar}^+$  laser; output powers at the

sample are set at 500 mW. Sample alignment is monitored by checking scattered light intensity from the host ground state  $\nu_1$  vibration; typical intensities are 100,000 cps for host  $\nu_1$ , 1,000 cps for the  $4,000\text{ cm}^{-1}$   $A_{1g}$   $\text{OsF}_6$  electronic origin, 100 cps for the  $\text{OsF}_6$   $\nu_1$  vibration built on this origin. The scattered light is filtered by a 1/2 meter double monochromator with 1,800 gr/mm gratings and detected by a low dark count, high sensitivity photomultiplier tube. The monochromator is scanned by a Hewlett-Packard 9845A desktop computer, which also collects, averages, and stores data.

## V. RESULTS AND DISCUSSION

### A. Absorption Spectra

#### $17,000\text{ cm}^{-1}$ $A_{1g}$ State

A summary of experimental frequencies and assignments for the band are given in Table III. While the 77°K spectra are complicated by hot band structure, the 4.2°K trace of the  $A_{1g}$  electronic state in the visible, shown in Figure 3, is rather simple and exhibits many characteristics of metal hexafluoride systematics.

The sharp origin [Full-Width Half Height (FWHH) =  $1\text{ cm}^{-1}$ ], moderately intense due to the forced electric dipole nature of the transition, is surrounded by sharp, weak features [ $\Delta E = +5$  to  $-5\text{ cm}^{-1}$ ] which are assumed to be due to pair structure. While no concentration studies were attempted, this structure roughly mimics the

pair structure built on the  $A_{1g}$  origin at  $4,000\text{ cm}^{-1}$ , on which concentration studies were carried out.

The most prominent features, the odd, Herzberg-Teller (HT) active vibrations,  $\nu_6$ ,  $\nu_4$ ,  $\nu_3$ , are assigned because of their large intensities and through comparison with gas phase, ground state vibrational frequencies.

Two-particle transitions, simultaneous excitation of guest electronic state and host ground state vibration, appearing in this band as a broad shoulder to the blue of the  $\nu_3$   $\text{OsF}_6$  transition, involve both the  $\nu_3$  and  $\nu_1$  host vibrations. [See Table I for host vibrational frequencies]. High resolution, high dispersion spectra of this region yield the  $\text{OsF}_6$   $\nu_1$  transition, which is moderately weak and broad [FWHH  $\sim 3\text{ cm}^{-1}$ ] presumably due to interaction with the host vibrations. The validity of this  $\nu_1$  assignment, agreeing with gas phase data, is enhanced by the appearance of the binary combinations  $\nu_6 + \nu_1$ ,  $\nu_4 + \nu_1$ , and  $\nu_3 + \nu_1$ .

The fundamentals of the JT active vibrations,  $\nu_2$  and  $\nu_5$ , are not observed as a result of parity selection rules. The fundamental frequencies, however, can be learned from odd-even binary combinations. Thus, from the  $\nu_4 + \nu_5$  and  $\nu_3 + \nu_5$  bands, it is seen that  $h\nu_5^\circ = 220\text{ cm}^{-1}$ . Also, the weak feature at  $766\text{ cm}^{-1}$  is assigned as a combination of host  $\nu_6$  and  $\text{OsF}_6$   $\nu_2$ , yielding  $h\nu_2^\circ = 626\text{ cm}^{-1}$ . These values for  $\nu_2$  and  $\nu_5$  can be used to gauge the strength of JT

interactions in the degenerate states, since it is expected that vibrational frequencies differ little between electronic ligand-field states.

Finally, no evidence of  $\nu_1$  progressions is seen, indicating similar geometries in ground and excited states. This is consistent with  $\text{ReF}_6$  and  $\text{IrF}_6$  data.<sup>3-7</sup>

4,000  $\text{cm}^{-1}$  ( $A_{1g} + T_{1g}$ ) Electronic Band

Spectra for this band were obtained for 1/2% and 1%  $\text{OsF}_6/\text{MoF}_6$  and  $\text{OsF}_6/\text{WF}_6$  samples at 77°K, 4.2°K and 1.8°K. Figure 4 shows a survey trace at 4.2°K. Table IV gives frequencies and assignments.

While there is little or no difference between 1.8 and 4.2°K spectra, two major differences are seen between 77°K and low temperature spectra. The high temperature spectra are broad, with origins of 3-5  $\text{cm}^{-1}$  FWHH, presumably because the  $T_{1g}$  JT active potential surface is coupled to thermally populated host phonons; also, transitions are relatively weak with intensity distributed over several hot bands. On the other hand, the low temperature spectra show sharp features, with origins of 1  $\text{cm}^{-1}$  FWHH, having somewhat more intensity and no hot band structure. Figure 5 compares origin regions at 77°K and 4.2°K.

Figure 6 compares the origin region for 1/2%  $\text{OsF}_6/\text{WF}_6$  and 1%  $\text{OsF}_6/\text{MoF}_6$  at 4.2°K. Of the four strong transitions present, the lowest in energy has pair structure built on it. Such an

assignment is evident of the non-linear relationship between  $\text{OsF}_6$  concentration and the fine structure intensity. This would imply, based on selection rules, that this lowest transition is the  $A_{1g}$  origin, for one origin component of a degenerate electronic state is unlikely to carry pair structure while its partners do not. The remaining three features are assigned as being the components of the  $T_{1g}$  origin split by low symmetry crystal field of the solid. These assignments are supported by the Raman data presented in the next section. It should also be noted that the four transitions are shifted, relative to each other, in the different hosts as shown in Figure 6.

Assuming the lowest energy transition is the  $A_{1g}$  origin, it is straightforward to assign associated vibronic structure, as there is a strong resemblance to the visible  $A_{1g}$  band. No coupling between  $A_{1g}$  and  $T_{1g}$  states is apparent; this is not altogether unexpected for in the free molecule  $O_h$  configuration, inter-state vibronic coupling is group theoretically forbidden.

The low-temperature spectra of 1/2%  $\text{OsF}_6/\text{WF}_6$  and 1%  $\text{OsF}_6/\text{MoF}_6$  are nearly identical. Vibrations  $\nu_6$ ,  $\nu_4$ ,  $\nu_3$ , and  $\nu_1$  are identified at 205, 275, 715, and  $726\text{ cm}^{-1}$ , respectively. No evidence of  $\nu_2$  or  $\nu_5$  fundamentals is found; in the  $\text{WF}_6$  spectra the binary combination  $\nu_4 + \nu_5$  gives the  $\nu_5$  fundamental as  $217\text{ cm}^{-1}$ . Combinations  $\nu_6 + \nu_1$  and  $\nu_4 + \nu_1$  are seen in both cases. Two-particle

transitions, involving host  $\nu_4$ ,  $\nu_3$ , and  $\nu_1$  vibrations, obviously at different energies, are seen in both hosts. Vibrational site splittings are similar in both hosts: 1-5  $\text{cm}^{-1}$  and 1.5-4  $\text{cm}^{-1}$  in  $\text{MoF}_6$  and  $\text{WF}_6$  for  $\nu_6$  and  $\nu_4$ , while no splitting on  $\nu_3$  is seen in either host. Finally, pair structure is carried on  $\nu_4$  and  $\nu_6$  in  $\text{WF}_6$ . The  $\nu_6$  pair structure in  $\text{MoF}_6$  is most likely masked by the host broadened nature of the  $\nu_6$  transition. The fact that this pair structure is observed on the false origins is indicative of a ground state dimer interaction.<sup>17</sup>

The  $T_{1g}$  portion of the 4,000  $\text{cm}^{-1}$  band is best analyzed by separating it into bending ( $\Delta E = 0-500 \text{ cm}^{-1}$ ) and stretching ( $\Delta E = 500-800 \text{ cm}^{-1}$ ) regions. The former is characterized by the crystal field split  $\nu_6$  false origin at 210  $\text{cm}^{-1}$ . The expected intense  $\nu_4$  false origin is absent; however, very weak structure is present at ca. 275  $\text{cm}^{-1}$ , and energetics suggest this is  $\nu_4$ . More discussion of this point will follow. Figure 7 contains these features.

There is a great deal of host-independent structure in the region between 40 and 500  $\text{cm}^{-1}$ . The host-independent nature of these features is verified by comparison of spectra taken in both hosts; moreover, these features are not explained by metal hexafluoride systematics as characterized in the  $A_{1g}$  electronic spectra. The most intense peaks, located at approximately 40, 120, 465 and 525  $\text{cm}^{-1}$ , are shown in Figure 8. The first of these,



the most intense of the four, has a FWHH of  $10 \text{ cm}^{-1}$ ; the possibility exists that this broad nature is due to the addition of host phonons on both the  $A_{1g}$  and  $T_{1g}$  origin components. It is seen in Figure 8 that this peak, though broad, is a singlet; the remaining three are obviously triplets, especially the one at  $465 \text{ cm}^{-1}$ .

Inspection of Englman's<sup>11</sup> calculation suggests that these features could result from a large,  $T_1 \otimes t_2$  LJTE with  $L/\sqrt{6} \hbar\omega^\circ \approx 2.0$ . Accordingly, the symmetry of these states would be  $A_2$ ,  $T_2$ ,  $T_1$  and  $T_1$ , associated with vibrational principal quantum numbers,  $n$ , of 1,1,3, and 3. Other features in the bending region, though less intense, are seen to fit this concept of a LJTE. Indeed, we find that, though part of this region is partially obscured by the  $\nu_6-\nu_4$  false origins, we are able to assign the majority (13) of the theoretical levels (up to  $n=3$ ) to experimental data. A linear least squares fitting routine, used to maximize this fit, indicates  $L/\sqrt{6} \hbar\omega^\circ = 1.8$ ,  $D = 2.16$ . A value of  $215 \text{ cm}^{-1}$  was used for  $\hbar\omega_5^\circ$ . The standard deviation of this fit is  $\sim 12 \text{ cm}^{-1}$ . A comparison of calculated and experimental energies is shown in Table V.

It is interesting to note that the three intense degenerate states shown in Figure 8 are split on the order of  $4\text{-}9 \text{ cm}^{-1}$  by the solid; the origin and  $\nu_6$  vibration are split by roughly

25 and 15  $\text{cm}^{-1}$ , respectively. This quenching of the low symmetry crystal field in JT states has been reported previously for the  $\Gamma_8 \otimes (e_g + t_{2g})$  JTE in  $\text{ReF}_6$ .<sup>7</sup>

It should be stressed that the assignments leading to this fit were, for the most part, numerically obtained through energetics, and a LJTE, while evidently dominant, is not necessarily the only mechanism present. As mentioned in Section I, quadratic terms become important for a  $\Gamma_8 \otimes (e_g + t_{2g})$  JTE. For a  $\Gamma_8$  electronic state, the LJT Hamiltonians have higher than molecular symmetry,<sup>10</sup> spherical for  $\Gamma_8 \otimes t_{2g}$  and cylindrical for  $\Gamma_8 \otimes e_g$ ; the quadratic Hamiltonians do not possess this pseudo-symmetry. Therefore, introduction of quadratic terms in the vibronic Hamiltonian for  $\Gamma_8$  states leads to a reduction of the vibronic symmetries and a concomitant higher number of observed states. It is only necessary to count the number of vibronic transitions to detect the presence of a quadratic effect for  $\Gamma_8$  states. However, for  $T_{1g}$  states, as in  $\text{OsF}_6$  and  $\text{UF}_6$ , both linear and quadratic Hamiltonians possess octahedral symmetry only. There is no reduction in vibronic symmetry upon introduction of quadratic terms in the Hamiltonian and, consequently, no qualitative method to detect the influence of a quadratic effect. It is possible, therefore, that a quadratic effect may be present in the  $T_{1g}$  state. However, the data convincingly indicate a strong

linear effect; a quadratic effect can only be shown to contribute by a parametric calculation and, to date, the secular matrix needed for this calculation has not been constructed.

As mentioned in Section I, a dominant  $T_{1g} \leftrightarrow t_{2g}$  LJTE has been shown to exist in  $UF_6$  also. In this case the data, though not precluding a quadratic effect, only required a linear vibronic coupling Hamiltonian to be fit.

The low intensity of the  $\nu_4$  false origin for the  $T_{1g}$  can be understood in light of this JT interpretation. It is likely that there is a crystal-induced Fermi resonance between  $\nu_4$  and the nearby  $A_2$  and  $T_2$  Jahn-Teller components of  $\nu_5$ . Although not seen in  $ReF_6$ ,  $IrF_6$ , and the other  $OsF_6$  states discussed in this paper, the mixing of  $\nu_4$  character into the  $\nu_5$  JT manifold probably is responsible for the large intensities of several of the  $\nu_5$  components. Another possible mechanism, a pseudo-JT effect seems unlikely; not only is it forbidden in zeroth order, but no perturbation of the  $4,000\text{ cm}^{-1}$   $A_{1g}$  band is observed in the spectra.

The stretching region of the  $T_{1g}$  band, shown in Figure 9, is rich in structure. Most of it is assignable to the  $A_{1g}$  electronic state as described earlier. The following are observed, however:  $\nu_3$  of the host in both  $MoF_6$  and  $WF_6$  and  $\nu_1$  of  $OsF_6$  built on one of the  $T_{1g}$  origin components. Conspicuously absent are: the  $OsF_6$   $\nu_3$  false origin in either host or evidence of  $\nu_2$  either as a

fundamental or in a binary combination. The remaining structure in the stretching region is assigned, however, by default, to the  $\nu_3/\nu_2$  manifold.

The nature of the data rules out any  $T_{1g} \leftrightarrow e_g$  analysis. The absence of  $\nu_3$  may be due, in a fashion similar to the  $\nu_5/\nu_4$  interaction, to an interaction between the components of  $\nu_2$  and  $\nu_3$ .

Analysis of the hot band structure (see Fig. 5) leads to an assignment of the ground and first excited electronic states levels. There are three hot bands to the red of the  $A_{1g}$  origin. That these are built on this transition is verified by Raman data.

Since  $OsF_6$  possess  $C_s$  site symmetry,<sup>17</sup> it is expected that the degeneracies of both the  $E_g$  and  $T_{2g}$  states would be fully removed. The presence of 3 instead of 4 hot bands indicates that an  $E_g$  and a  $T_{2g}$  component are accidentally degenerate. Accordingly, four models may be proposed, one with an  $E_g$  ground state, the others with a  $T_{2g}$  ground state. These are shown in Figure 10 along with their appropriate Boltzmann factors for 77°K.

Experimentally, the intensities of the  $A_{1g}$  origin transition and the second hot band are equal, while hot bands 1 and 3 are equal in intensity. The former are 10 times as intense as the latter. Assuming equal transition moments for transitions

originating from (low symmetry) components of the same state, model (b) predicts that hot band 1 should be 3/4 as intense as the origin transition, based on Boltzmann factors. This model is ruled out, therefore, as the actual intensity ratio is 0.1. Model(c) predicts that hot band 1 should have equal or greater intensity than the origin transition and therefore, can also be eliminated. Finally, model (d) predicts that hot bands 2 and 3 should be of similar intensities, thereby also eliminating it. The only model that cannot be conclusively ruled out by the data is (a). This model is even more attractive if the  $A_{1g} \leftarrow E_g$  transition moment is assumed to be much larger than the  $A_{1g} \leftarrow T_{2g}$  moment. The low lying electronic states are summarized as follows: the  $E_g$  state is assigned as the ground electronic state with a site splitting of  $28\text{ cm}^{-1}$ ; the  $T_{2g}$  state is the first excited electronic state; and the  $T_{2g}$  state is resolved into components at 14, 28, and  $40\text{ cm}^{-1}$ . Such an assignment is further corroborated by the expected hot bands on the  $T_{1g}$  origin being superimposed on the existing  $A_{1g}$  origin and its hot bands as is shown in Figure 5.

$8,000\text{ cm}^{-1}$  Band ( $T_{2g} + E_g$ )

This band violates the systematics seen in other low temperature absorption spectra of  $\text{ReF}_6$ ,  $\text{IrF}_6$ , and  $\text{OsF}_6$ . A survey spectrum of the entire region is shown in Figure 11. The spectrum,

comprised of an envelope of transitions covering  $800\text{ cm}^{-1}$ , can be qualitatively interpreted in the following manner. There is one origin with strong features at 120, 250, and  $660\text{ cm}^{-1}$ . These are presumably the  $\nu_6$ ,  $\nu_4$ , and  $\nu_3$  false origins. Note the discrepancies between these numbers and the frequencies measured in the two  $A_{1g}$  states and even the  $T_{1g}$  state. Other transitions, of the same magnitude of intensity as the false origins, at  $320$  and  $460\text{ cm}^{-1}$ , are unassignable using known energetics. A weak feature at  $719\text{ cm}^{-1}$  is assigned as  $\nu_1$ . Finally, no possible interpretation of these transitions in terms of metal hexafluoride systematics results in reasonable locations for the missing origin components and more comprehensible values for false origin frequencies.

The absence of 4 of the 5 expected origin components is not due to selection rules. This judgment is based on two facts: no origin component of any degenerate electronic state is missing in any other low temperature spectra of  $\text{IrF}_6$ ,  $\text{ReF}_6$ , or  $\text{OsF}_6$ , and the reduction of molecular symmetry by the solid ( $C_s$  site symmetry) tends to relax selection rules.

The quenching of electronic operators within ground or excited vibronic manifolds is well known.<sup>18,19,20</sup> One such operator is the low symmetry crystal field. Indeed, such an effect has been characterized in  $\text{ReF}_6$  excited vibronic states.<sup>7</sup>

The complexity of the  $8,000 \text{ cm}^{-1}$  band structure indicates that both  $E_g$  and  $T_{2g}$  states are strongly involved in vibronic coupling. It is, therefore, interesting to examine the influence of a LJT effect on the crystal field splitting of the  $E_g$  and  $T_{2g}$  states.

The ground vibronic state Hamiltonians for these states are listed below.<sup>18,20</sup>

Only low symmetry operators are included.

I.  $E \otimes e$  LJTE

$$H = G(A_1) \frac{I}{2} + q G(E_\theta) \sigma_\theta$$

$$I = \begin{pmatrix} 1 & 0 \\ 0 & 1 \end{pmatrix} \sigma_\theta = \begin{pmatrix} -1 & 0 \\ 0 & 1 \end{pmatrix}$$

II.  $T \otimes e$  LJTE

$$H = G(A_1) \frac{I}{2} + G(E_\theta) \epsilon_\theta + K(T_2) [G(\xi) T_\xi + G(\eta) T_\eta + G(\zeta) T_\zeta]$$

$$I = \begin{pmatrix} 1 & 0 & 0 \\ 0 & 1 & 0 \\ 0 & 0 & 1 \end{pmatrix}; \quad \epsilon_\theta = \begin{pmatrix} \frac{1}{2} & 0 & 0 \\ 0 & \frac{1}{2} & 0 \\ 0 & 0 & -\frac{1}{2} \end{pmatrix}$$

$$T_\xi = -\begin{pmatrix} 0 & 0 & 0 \\ 0 & 0 & 1 \\ 0 & 1 & 0 \end{pmatrix}; \quad T_\eta = -\begin{pmatrix} 0 & 0 & 1 \\ 0 & 0 & 0 \\ 1 & 0 & 0 \end{pmatrix}; \quad T_\zeta = -\begin{pmatrix} 0 & 1 & 0 \\ 1 & 0 & 0 \\ 0 & 0 & 0 \end{pmatrix}$$

III.  $T \otimes t_2$  LJTE

$$H = G(A_1) \frac{I}{2} + K(E) G(E_\theta) \epsilon_\theta + K'(T_2) [G(\xi) T_\xi + G(\eta) T_\eta + G(\zeta) T_\zeta]$$

The operators represent the following solid state effects:  $G(A_1) \frac{1}{2}$ , gas to crystal shifts;  $G(E_g)\sigma_g$  and  $G(E_g)\epsilon_g$ , tetragonal ( $D_{4h}$ ) distortion;  $G(\xi)T_\xi$ ,  $G(\eta)T_\eta$ , and  $G(\zeta)T_\zeta$ , trigonal ( $D_{3d}$ ) distortion. The G's are parameters expressing the size of the low symmetry crystal field. Finally,  $q$ ,  $K(T_2)$ ,  $K(E)$  and  $K'(T_2)$  are quenching factors which are dependent on the magnitude of the JTE.

These quenching factors have been calculated for LJT effects.<sup>20</sup>

1.  $0.484 \leq q \leq 0.500$
2.  $K(T_2) = \exp[-L^2/(2\hbar\omega)^2] = \exp[-3E_{JT}/(2\hbar\omega)]$
3.  $K(E) \equiv \exp[-9E_{JT}/(4\hbar\omega)]$
4.  $K'(T_2) \equiv \frac{1}{3}(2 + \exp[-9E_{JT}/(4\hbar\omega)])$

As can be seen, the tetragonal distortion related splitting of an E vibronic ground state is not eliminated by a  $E \otimes e$  linear effect. However, in a T electronic state, for  $T \otimes e$  linear effect, a trigonal distortion can be reduced to zero for a large interaction, while a tetragonal distortion is unaffected. Finally, for a  $T \otimes t$  effect, a tetragonal distortion caused splitting is brought to zero for a large coupling, while the trigonal field related splitting is reduced to 2/3 of its value in the absence of a JTE. For example, for  $E_{JT} = \hbar\omega$ ,  $K(E) = .11$  and  $K'(T_2) = .78$ ; where  $E_{JT} = 2\hbar\omega$ ,  $K(E) = .01$  and  $K'(T_2) = .68$ .



O'Brien<sup>21</sup> has also shown that  $K(E) = K(T_2)$  for a T state coupled equally to both  $e_g$  and  $t$  modes and that  $1.0 > K(E)$ ,  $K(T_2) > 0.4$ . Therefore, no T state origin splitting can be completely quenched in the case of equal  $T \otimes e$  and  $T \otimes t_2$  JT interactions.

Assuming that  $OsF_6$  has either  $D_{4h}$  or  $C_5$  symmetry in the crystal,<sup>17</sup> the latter expressed as a sum of tetragonal and trigonal distortions, it is apparent that no linear effect can be responsible for a total quenching of origin crystal field splittings resulting in the observation of only one origin transition. We are thus unable to explain the absence of the other expected origin transitions.

#### B. Electronic Raman Spectra

Attempts were made to obtain Raman scattering spectra of the  $8,000\text{ cm}^{-1}$ ,  $4,000\text{ cm}^{-1}$ , and first excited electronic states, along with the upper component of the  $E_g$  ground state. Of these, only spectra of the  $4,000\text{ cm}^{-1}$  band were observed. A survey spectrum at  $77^\circ\text{K}$  is shown in Figure 12. Three features are present, an intense origin (1000 cps) along with weak structure at  $250\text{ cm}^{-1}$  (30 cps) and at  $700\text{ cm}^{-1}$  (100 cps). These are apparently the even vibrations  $\nu_5$ , and/or  $\nu_2$ , and  $\nu_1$ .

At higher resolution, the origin is seen to consist of four transitions, as illustrated in Figure 13; at  $4.2^\circ\text{K}$ , only the transition highest in energy is observed. This latter feature

corresponds energetically to the  $A_{1g}$  origin in the absorption spectra and is so assigned. One vibrational peak is seen at 4.2°K; this feature, at  $725\text{ cm}^{-1}$ , is obviously the totally symmetric vibration built on the  $A_{1g}$  origin. The value of  $\hbar\omega = 725\text{ cm}^{-1}$  is quite close to the value of  $\nu_1$  observed in the absorption spectra. A summary of high and low temperature data is presented in Table VI.

The hot band structure associated with the origin corresponds to the hot band structure to the red of the  $A_{1g}$  origin in the 77°K absorption spectra. Accordingly, these features can be assigned to the transitions to the  $A_{1g}$  origin from the thermally populated upper component of the  $E_g$  ground state at  $28\text{ cm}^{-1}$  and the 3  $T_{2g}$  first excited state components at 14, 28, and  $40\text{ cm}^{-1}$ . This gives an unperturbed approximate value of  $30\text{ cm}^{-1}$  for the separation of ground and first excited states, consistent, at least qualitatively, with Eisenstein's calculation. Also, the two components at  $28\text{ cm}^{-1}$  are accidentally degenerate in both  $\text{MoF}_6$  and  $\text{WF}_6$  hosts indicating the shift in them due to change in hosts is within the linewidth [ $\text{FWHM} \sim 7\text{ cm}^{-1}$ ] of the Raman transition.

## VI. CONCLUSIONS

Absorption and electronic Raman spectroscopy have been used to locate and study the electronic state of  $\text{OsF}_6$ . It is

found that previous electronic calculations are substantially correct. See Table I for comparison of low temperature data and calculational results. These data agree with Eisenstein's predictions of an  $E_g$  ground state and a  $T_{2g}$  first excited state nearly degenerate with it, and an  $A_{1g} + T_{1g}$  band at roughly  $4,000\text{ cm}^{-1}$  with the  $A_{1g}$  state being slightly lower in energy. Spectra of the  $8,000\text{ cm}^{-1}$  band, however, do not explicitly show the presence of the predicted  $T_{2g} + E_g$  origins and bands. The band observed violates  $MF_6$  systematics, however, and it seems likely that it is heavily perturbed by vibronic coupling. The absence of expected origin transitions is not understood. Linear (or quadratic) Jahn-Teller effects alone do not seem responsible. Finally, we observe an  $A_{1g}$  electronic state at  $16,900\text{ cm}^{-1}$  as predicted.

The two  $A_{1g}$  electronic state spectra are nearly identical in appearance and exhibit hexafluoride systematics. The  $A_{1g}$  states are characterized by:

1. one moderately intense origin with associated pair structure.
2. intense false origins,  $\nu_6$ ,  $\nu_4$ , and  $\nu_3$ .
3. a rather weak  $\nu_1$  transition.
4.  $\nu_2$ ,  $\nu_5$  not directly observed; identified, if at all, by binary combination energies.
5. low symmetry crystal field splittings of degenerate  $\nu_6$ ,  $\nu_4$ .

and  $\nu_3$  are  $\sim 5 \text{ cm}^{-1}$ .

6. vibrational energies essentially unchanged between states; gas-crystal vibrational shifts are small.
7. two particle transitions identified for  $\nu_6$ ,  $\nu_4$ , and  $\nu_3$ .
8. pair structure carried on the false origins indicating that dimer interactions are present in ground state.

It is found that the  $T_{1g}$  electronic state is involved in a dominant  $T_{1g} \otimes t_{2g}$  LJTE with  $D \sim 2.2$ . A crystal induced Fermi resonance is observed between  $\nu_4$  and  $\nu_5$  JT components. This interaction apparently affects the intensity of several  $\nu_5$  components. Its affect on the  $\nu_5$  component energies is not known but appears to be small as indicated by the overall good fit between JT calculations and the experimental results. Finally, this dominant linear effect agrees with the dominant linear  $T_{1g} \otimes t_{2g}$  effect reported for  $UF_6$ ; on the other hand, quadratic effects have been reported for the  $\Gamma_8$  states of  $ReF_6$  and  $IrF_6$ .

REFERENCES

1. B. Weinstock, H.H. Claassen, and J.G. Malm, J. Chem. Phys. 32, 181 (1958).
2. W. Moffitt, G.L. Goodman, M. Fred, and B. Weinstock, Mol. Phys. 2, 109 (1959).
3. E.R. Bernstein and J.D. Webb, Mol. Phys. 37, 191 (1979).
4. E.R. Bernstein and J.D. Webb, Mol. Phys. 36, 1113 (1978).
5. E.R. Bernstein and J.D. Webb, Mol. Phys. 35, 1585 (1978).
6. E.R. Bernstein and J.D. Webb, Mol. Phys. 37 203 (1979).
7. Meredith, G.R., J.D. Webb, and E.R. Bernstein, Mol. Phys. 34, 995 (1977).
8. E.R. Bernstein, G.R. Meredith, and J.D. Webb, J. Chem. Phys. 68, 4066 (1978).
9. J.C. Eisenstein, J. Chem. Phys. 34, 310 (1961).
10. W. Moffitt and W. Thorson, Phys. Rev. 108, 1251 (1957).
11. R. Englman, M. Caner, and S. Toaff, J. Phys. Soc. Japan 29, 306 (1970).
12. J.S. Griffith, The Irreducible Tensor Method for Molecular Symmetry Groups (Prentice-Hall, London, 1962).
13. S.L. Altmann and A.P. Cracknell, Rev. Mod. Phys. 37, 19 (1965).
14. E.R. Bernstein and G.R. Meredith, J. Chem. Phys. 64, 375 (1976).
15. D.L. Michalopoulos, Ph.D. Thesis (Colorado State University, 1982).
16. B. Weinstock and J.C. Malm, J. Am. Chem. Soc. 80, 4466 (1958).
17. E.R. Bernstein and J.R. Meredith, J. Chem. Phys. 64, 395 (1976).
18. F.S. Ham, Electron Paramagnetic Resonance, ed. S. Geschwind (Plenum Press, New York, 1972), p.1.
19. M.D. Sturge, Solid State Physics, ed. F. Seitz, D. Turnbull, and H. Ehrenreich, (Academic Press, New York, 1967), Vol. 20, P. 91.
20. R. Englman, The Jahn Teller Effect in Molecules and Crystals, (Wiley-Interscience, London, 1972) pp. 19-124.
21. M.C.M. O'Brien, Phys. Rev. 187, 407 (1969).
22. E.R. Bernstein and G.R. Meredith, Chem. Phys. 24, 289 (1977).

TABLE I

Ground state vibrational energies for  $\text{OsF}_6$ ,  $\text{MoF}_6$ , and  $\text{WF}_6$ .  $\text{OsF}_6$  energies measured at room temperature with gas and liquid samples [Ref. 1].  $\text{MoF}_6$ ,  $\text{WF}_6$  energies measured at 77°K with neat crystals [Ref. 22]; values shown here are averaged values of exciton energies. The stretching region includes  $\nu_1$ ,  $\nu_2$ , and  $\nu_3$ ; the bending region includes  $\nu_4$ ,  $\nu_5$ , and  $\nu_6$ .

	$\nu_1(a_{1g})$	$\nu_2(e_g)$	$\nu_3(t_{1u})$	$\nu_4(t_{1u})$	$\nu_5(t_{2g})$	$\nu_6(t_{2u})$
$\text{OsF}_6$	733	632	720	268	252	200
$\text{MoF}_6$	742	645	718	265	320	140
$\text{WF}_6$	772	670	690	250	325	147

TABLE II

Comparison of calculated and experimental electronic energies. Moffitt's calculation employed a spherical basis and states are labeled by angular momentum quantum numbers  $J$ ; Eisenstein's calculation employed the  $O_h$  symmetry of the molecule and states are labeled by  $O_h$  point group representation. Note the correlation between the  $J=2$  state of Moffitt and the ( $E_g + T_{2g}$ ) states of Eisenstein. Low temperature energies are corrected for approximate gas-to-crystal shifts to obtain free molecule energies. All energies are expressed as  $\text{cm}^{-1}$ .

STATES		CALCULATIONS		EXPERIMENTS	
$O_h$	$R_3$	Moffitt <sup>a</sup>	Eisenstein <sup>b</sup>	298°K <sup>c</sup>	4.2°K <sup>d</sup>
$E_g$	2	0	0	0	0
$T_{2g}$			122	<250	~100
$T_{1g}$	1	3,900	4,305	4,316	4,310
$A_{1g}$	0	4,270	4,327	4,371	4,370
$T_{2g}$	2	8,170	8,670	8,482	8,480
$E_g$			8,826	---	
$A_{1g}$	0	16,300	17,383	17,301	17,300

a. ref. 10

b. ref. 9

c. ref. 10

d. ref. this work

TABLE III

Summary of absorption data for  $16,900\text{ cm}^{-1}$   $A_{1g} \leftarrow E_g$  electronic transition at  $4.2^\circ\text{K}$ . Sample used was a 1%  $\text{OsF}_6/\text{MoF}_6$  mixed crystal. Uncertainties are  $\pm 0.2\text{ cm}^{-1}$ .

$\text{cm}^{-1}(\text{VAC})$	FWHH <sup>a</sup>	I <sup>b</sup>	$\Delta E(0-0)(\text{cm}^{-1})^c$	Assignments
16,912.55	1 $\text{cm}^{-1}$	W	-5.42	pairs + 0-0
16,915.54		W	-2.43	pairs + 0-0
16,917.97	1 $\text{cm}^{-1}$	S	0	0-0
16,918.84		M	0.87	pairs + 0-0
16,920.55	1 $\text{cm}^{-1}$	VW	2.58	pairs + 0-0
16,922.53		W	4.56	pairs + 0-0
17,115.23	2.1 $\text{cm}^{-1}$	W	197.26	pairs + $\nu_6$
17,117.60		S	199.63	$\nu_6$
17,119.16	2.1 $\text{cm}^{-1}$	S	201.19	$\nu_6$
17,121.52		VW	203.55	pairs + $\nu_6$
17,123.48	3 $\text{cm}^{-1}$	VW	205.51	pairs + $\nu_6$
17,189.38		M	271.03	$\nu_4$
17,193.93	3 $\text{cm}^{-1}$	S	275.96	$\nu_4$
17,196.25		MS	278.28	$\nu_4$
17,409.02	3 $\text{cm}^{-1}$	MW	491.02	$\nu_4 + \nu_5$ ; $\nu_5=215.06\text{ cm}^{-1}$
17,611.54		S	693.57	$\nu_3$
17,613.43	3 $\text{cm}^{-1}$	S	695.46	$\nu_3(\text{h})^d$
17,631.91		W	713.94	$\nu_3(\text{h})$
17,646.67	3 $\text{cm}^{-1}$	M	728.70	$\nu_1$
17,657.17		VW	739.20	$\nu_1(\text{h})$
17,684.16		W	766.19	$\nu_6(\text{h})+\nu_2$ ; $\nu_2=626.19\text{ cm}^{-1}$



TABLE III (cont.)

$\text{cm}^{-1}(\text{VAC})$	FWHH	I	$\Delta E(0-0)(\text{cm}^{-1})$	Assignments
17,834.77		MW	916.80	$\nu_3 + \nu_5$ ; $\nu_5 = 223.23 \text{ cm}^{-1}$
17,849.35		MW	931.38	$\nu_6 + \nu_1$
17,911.31		MW	993.34	$\nu_4(\text{h}) + \nu_1(\text{h})$
17,925.37		MW	1,007.40	$\nu_4 + \nu_1$
18,339.86		MW	1,421.89	$\nu_3 + \nu_1$

Footnotes

- a. FWHH = Full Width Half Height
- b. I = Intensity  
 VW = Very Weak  
 MW = Moderately Weak  
 W = Weak  
 M = Medium  
 MS = Moderately Strong  
 S = Strong  
 VS = Very Strong
- c.  $\Delta E(0-0)$  energy differences measured relative to origin transition.
- d. h = host

TABLE IV

Summary of absorption data for  $(A_{1g} + T_{1g}) \leftarrow E_g$  electronic transition at  $4,000 \text{ cm}^{-1}$  at  $4.2^\circ\text{K}$ . Sample used was a 1%  $\text{OsF}_6/\text{MoF}_6$ . Uncertainties are  $\pm 0.1 \text{ cm}^{-1}$ . See Table III for notation used. An  $A_{1g}$  or  $T_{1g}$  in the assignment column indicates the origin on which the transition is built. Vibronic symmetries are given in parentheses. All  $T_{1g}$  transition energies are measured from an average origin energy of  $4,112.56 \text{ cm}^{-1}$ .

$\text{cm}^{-1}(\text{VAC})$	FWHH	I	$\Delta E(0-0)(\text{cm}^{-1})$	Assignments
4,078.13	.6	M	-8.34	$A_{1g} + \text{pairs}$
4,080.47		W	-6.00	$A_{1g} + \text{pairs}$
4,083.13		W	-3.34	$A_{1g} + \text{pairs}$
4,084.72		W	-1.75	$A_{1g} + \text{pairs}$
4,086.47	1.7	S	0	$A_{1g} (0-0)$
4,088.31	1.1	M	1.84	$A_{1g} + \text{pairs}$
4,089.40		M	2.93	$A_{1g} + \text{pairs}$
4,096.52	.9	W	10.05	$A_{1g} + \text{pairs}$
4,098.70	.5	M	0	$T_{1g}$ origin
4,112.10	.6	S	0	$T_{1g}$ origin
4,126.87	.9	S	0	$T_{1g}$ origin
4,153.45	7.5	S	40.89	$T_{1g} + \nu_5(A_2)$
4,231.86		M	119.30	$T_{1g} + \nu_5(T_2)$
4,233.75		M	121.19	$T_{1g} + \nu_5(T_2)$
4,235.90		W	123.34	$T_{1g} + \nu_5(T_2)$
4,288.04		S	201.57	$A_{1g} + \nu_6 + \text{pairs}$
4,290.80	2.4	S	204.33	$A_{1g} + \nu_6$
4,291.91	6.0	S	205.44	$A_{1g} + \nu_6$

TABLE IV (cont.)

$\text{cm}^{-1}$ (VAC)	FWHH	I	$\Delta E(0-0)(\text{cm}^{-1})$	Assignments
4,297.81	4.6	S	211.34	$A_{1g} + \nu_6$
4,300.96		M	214.49	$A_{1g} + \nu_6 + \text{pairs}$
4,314.13	3.3	S	201.57	$T_{1g} + \nu_6$
4,323.56	5.4	S	211.00	$T_{1g} + \nu_6$
4,327.86	4.8	S	215.30	$T_{1g} + \nu_6$
4,338.85		M	252.38	$A_{1g} + \nu_4(h)$
4,343.37		M	256.90	$A_{1g} + \nu_4(h)$
4,348.19		M	261.72	$A_{1g} + \nu_4(h)$
4,352.26		S	265.79	$A_{1g} + \nu_4(h)$
4,355.11		M	268.64	$A_{1g} + \nu_4(h)$
4,358.05		S	271.58	$A_{1g} + \nu_4(h)$
4,362.33		S	275.86	$A_{1g} + \nu_4$
4,363.95		S	277.48	$A_{1g} + \nu_4$
4,366.71		S	280.24	$A_{1g} + \nu_4$
4,368.52		M	282.05	$A_{1g} + \nu_4$
4,385.19		W	272.63	$T_{1g} + \nu_4$
4,387.17		VW	274.61	$T_{1g} + \nu_4$
4,391.45		MW	278.89	$T_{1g} + \nu_4$
4,409.57		W	297.01	$T_{1g} + 2\nu_5(A_2)$
4,435.29		MW	322.73	$T_{1g} + 2\nu_5(T_2)$
4,443.18	3.5	M	330.62	$T_{1g} + 2\nu_5(T_1)$
4,500.18		W	387.62	$T_{1g} + 2\nu_5(T_2)$
4,576.82		W	464.26	$T_{1g} + 2\nu_5(T_1)$
4,579.23		W	466.67	$T_{1g} + 2\nu_5(T_1)$
4,583.11		W	470.55	$T_{1g} + 2\nu_5(T_1)$

TABLE IV (cont.)

$\text{cm}^{-1}(\text{VAC})$	FWHH	I	$\Delta E(0-0)(\text{cm}^{-1})$	Assignments
4,589.95		M	477.39	$T_{1g} + 3\nu_5(T_1)$
4,592.69	2.2	M	480.13	$T_{1g} + 3\nu_5(T_1)$
4,594.28		M	481.72	$T_{1g} + 3\nu_5(T_1)$
4,597.02		W	484.46	$T_{1g} + 3\nu_5(A_2)$
4,602.95		W	490.39	$T_{1g} + 3\nu_5(A_1)$
4,616.66		W	504.10	$T_{1g} + 3\nu_5(E)$
4,620.40		W	507.84	$T_{1g} + 3\nu_5(E)$
4,636.25	16.0	M	523.69	$T_{1g} + 3\nu_5(T_1)$
4,640.02	16.0	M	527.92	$T_{1g} + 3\nu_5(T_1)$
4,645.73	16.0	M	533.17	$T_{1g} + 3\nu_5(T_1)$
4,689.31		W	576.75	$T_{1g} + 3\nu_5(A_2)$
4,783.90	9.0	M	697.43	$A_{1g} + \nu_3(h)$
4,786.30	9.0	M	699.83	$A_{1g} + \nu_3(h)$
4,801.82	4.3	S	715.35	$A_{1g} + \nu_3$
4,804.82		W	718.35	$A_{1g} + \nu_3(h)$
4,812.34	1.0	M	725.87	$A_{1g} + \nu_1$
4,813.84		W	701.28	$T_{1g} + \nu_3(h)$
4,816.74		W	704.18	$T_{1g} + \nu_3(h)$
4,820.34		M	707.78	$T_{1g} + \nu_3(h)$
4,827.56	1.0	S	741.09	$A_{1g} + \nu_1(h)$
4,833.75		W	721.19	$T_{1g} + \nu_3/\nu_2$
4,836.90		W	724.34	$T_{1g} + \nu_3/\nu_2$
4,847.22		W	760.75	$A_{1g} + \nu_3(h) + \text{phonon}(66 \text{ cm}^{-1})$
4,850.63	5.0	MS	764.16	$A_{1g} + \nu_3(h) + \text{phonon}(66 \text{ cm}^{-1})$
4,853.22		M	766.75	$A_{1g} + \nu_3(h) + \text{phonon}(66 \text{ cm}^{-1})$

TABLE IV (cont.)

$\text{cm}^{-1}$ (VAC)	FWHH	I	$\Delta E(0-0)(\text{cm}^{-1})$	Assignments
4,863.85	10.0	MS	777.37	$A_{1g} + \nu_3(h) + \text{phonon}(83 \text{ cm}^{-1})$
4,867.40		M	780.93	$A_{1g} + \nu_3(h) + \text{phonon}(83 \text{ cm}^{-1})$
4,876.42		W	763.86	$T_{1g} + \nu_3/\nu_2$
4,883.09		W	770.53	$T_{1g} + \nu_3/\nu_2$
4,894.21		M	781.65	$T_{1g} + \nu_3/\nu_2$
4,934.92		W	822.36	$T_{1g} + \nu_3/\nu_2$
5,007.21	4.5	VS	920.74	$A_{1g} + \nu_6 + \nu_1$
5,015.63	3.0	M	903.07	$T_{1g} + \nu_3/\nu_2$
5,017.77		M	905.21	$T_{1g} + \nu_3/\nu_2$
5,038.13		M	925.57	$T_{1g} + \nu_3/\nu_2$
5,041.18		M	928.62	$T_{1g} + \nu_3/\nu_2$
5,047.67		W	935.11	$T_{1g} + \nu_3/\nu_2$
5,051.62		M	939.06	$T_{1g} + \nu_3/\nu_2$
5,055.45	8.8	S	942.89	$T_{1g} + \nu_3/\nu_2$
5,057.37		M	944.81	$T_{1g} + \nu_3/\nu_2$
5,077.92	11.3	S	991.45	$A_{1g} + \nu_4 + \nu_1$
5,079.08	11.3	S	992.61	$A_{1g} + \nu_4 + \nu_1$
5,081.66	11.3	S	995.19	$A_{1g} + \nu_4 + \nu_1$
5,085.54	11.3	M	999.07	$A_{1g} + \nu_4 + \nu_1$
5,089.04	11.3	M	1,002.57	$A_{1g} + \nu_4 + \nu_1$

TABLE V

Comparison of Englman, Caner, and Toaff's  $T_1 \leftrightarrow t_2$  LJT calculation for a molecule of O-symmetry and  $OsF_6$  transitions in the  $4,000\text{ cm}^{-1}$  band. A linear fitting routine was used to obtain a D of  $\sim 2.0$ . Spectra were taken at  $4.2^\circ\text{K}$  with a 1%  $OsF_6/MoF_6$  sample.

$\text{cm}^{-1}$ (VAC)	$\Delta E(0-0)^\dagger$	$\Delta E(\text{AVE})$	Calc.	Vibronic Symmetry	$n^\ddagger$
4,153.45	40.89		41.35	$A_2^\ddagger$	1
4,231.86	119.30	121.28	132.30	$T_2^\ddagger$	1
4,233.75	121.19				
4,235.90	123.34				
4,409.57	297.01		305.95	$A_2$	2
4,435.29	322.73		318.36	$T_2$	2
4,442.18	330.62		334.89	$T_1$	2
4,500.18	387.62		384.51	$T_2$	2
4,576.82	464.26	467.16	434.12	$T_1$	2
4,583.11	470.55				
4,589.95	477.39	479.75	442.39	$T_1^\ddagger$	3
4,592.69	480.13				
4,594.28	481.72				
4,597.02	484.46		454.80	$A_2$	3
4,602.95	490.39		463.06	$A_1$	3
4,616.66	504.10	505.97	487.87	E	3
4,620.40	507.84				
4,636.25	523.69	528.26	512.68	$T_1^\ddagger$	3
4,640.02	527.92				
4,645.73	533.17				
4,689.31	576.75		587.10	$A_2$	3

TABLE V (cont.)Footnotes

† measured from averaged origin energy of  $4,112.56 \text{ cm}^{-1}$

‡ transitions shown in figure

‡ principal vibrational quantum number

---

---

TABLE VI

Comparison of  $A_{1g} + E_g$  Raman scattering data for 77°K and 4.2°K. Sample is a 5%  $\text{OsF}_6/\text{MoF}_6$  mixed crystal. Slidewidths are on the order of  $5 \text{ cm}^{-1}$  for 77°K and  $10 \text{ cm}^{-1}$  for 4.2°K spectra due to low intensities of transitions. Energies are certain to  $\pm 0.2 \text{ cm}^{-1}$ . The origin and 3 hot bands of the 77°K spectra agree with infrared absorption data, as do the origin and  $\nu_1$  transition in the 4.2°K spectra.

Stokes Shift ( $\text{VAC cm}^{-1}$ )	FWHH	77°K		Assignments
		I	$\Delta E(0-0)$	
4,044.11		M	-44.90	hb, $T_{2g}$ 1st excited state
4,060.68	$7 \text{ cm}^{-1}$	S	-28.33	hb, $T_{2g}$ 1st excited state, $E_g$ ground state component
4,074.84		W	-14.17	hb, $T_{2g}$ 1st excited state
4,089.01	$7 \text{ cm}^{-1}$	S	0	$A_{1g}$ 0-0
4,297.02		W	208.01	$\nu_5 + \text{hb}$
4,328.49		W	239.48	$\nu_5 + \text{hb}$
4,353.54		W	264.53	$\nu_5 + \text{hb}$
4,386.45		W	297.44	$\nu_5 + \text{hb}$
4,418.11		W	329.10	$\nu_5 + \text{hb}$
4,764.05		W	675.04	$\nu_1 + \text{hb}$ ( $T_{2g}$ 1st excited state)
4,794.14		W	705.13	$\nu_1 + \text{hb}$ ( $T_{2g}$ 1st excited state)
4,804.85	$5 \text{ cm}^{-1}$	MW	715.84	$\nu_1$
<u>4.2°K</u>				
4,082.77		W	-7.06	pairs
4,089.83	$8.5 \text{ cm}^{-1}$	S	0	$A_{1g}$ 0-0
4,103.01		W	13.18	pairs
4,807.74	$8.5 \text{ cm}^{-1}$	MW	724.97	$\nu_1$



FIGURE CAPTIONSFigure 1

A schematic diagram showing the effect of an octahedral ligand field, spin orbit coupling, and electron correlation on a  $(d_{t_{2g}})^2$  electronic configuration. Note the predicted near degeneracies of the pairs of states at 0, 4,000, and 8,000  $\text{cm}^{-1}$ .

Figure 2

Jahn-Teller energies as a function of coupling parameter  $L_{\tau}$  for a  $T_2 \otimes t_2$  LJTE for a molecule of  $O$ -symmetry. Subscripts 1 and 2 should be interchanged for a  $T_1 \times t_2$  effect, e.g., the 4,000  $\text{cm}^{-1}$   $T_{1g}$  state of  $\text{OsF}_6$ . [Reproduced with permission, R. Englman, "The Jahn-Teller Effect in Molecules and Crystals", (Wiley Interscience, London, 1972) p. 72.]

Figure 3

Survey absorption spectrum for the 16,900  $\text{cm}^{-1}$   $A_{1g} \leftarrow E_g$  transition of  $\text{OsF}_6$  at 4.2°K using a 1%  $\text{OsF}_6/\text{MoF}_6$  sample. This spectrum exhibits many of the features characterizing hexafluoride systematics.

Figure 4

Survey absorption spectrum of the 4,000  $\text{cm}^{-1}$   $(A_{1g} + T_{1g}) \leftarrow E_g$  transition of  $\text{OsF}_6$  at 4.2°K using a 1%  $\text{OsF}_6/\text{MoF}_6$  sample. Note the complexity of the band as compared to the 16,900  $\text{cm}^{-1}$   $A_{1g}$  band due primarily to the presence of the  $T_{1g}$  state.

Figure 5

A comparison of the 4,000  $\text{cm}^{-1}$   $(A_{1g} + T_{2g})$  origin at 77°K and 4.2°K for a 1%  $\text{OsF}_6/\text{MoF}_6$  sample. Note the hot bands to the red of the  $A_{1g}$  origin. See text for the hot band analysis leading to ground and first excited electronic state assignments. The stick diagram shows that hot bands built on the  $T_{1g}$  origin components are superimposable on the other transitions in the figure. The weak features built on the  $A_{1g}$  origin are assigned as pair structure.

Figure 6

A comparison of  $4,000\text{ cm}^{-1}$  ( $A_{1g} + T_{1g}$ ) origin at  $4.2^\circ\text{K}$  for .5%  $\text{OsF}_6/\text{WF}_6$  and 1%  $\text{OsF}_6/\text{MoF}_6$  samples. The nonlinear relationship between  $\text{OsF}_6$  concentration and the fine structure intensity about the  $A_{1g}$  origin indicates the structure is due to pairs, etc.

Figure 7

The bending/false origin region of the  $4,000\text{ cm}^{-1}$  ( $A_{1g} + T_{1g}$ )  $\leftarrow E_g$  at  $4.2^\circ\text{K}$  for a 1%  $\text{OsF}_6/\text{MoF}_6$  sample. Note the weak intensity of the  $\nu_4$  false origin built on the  $T_{1g}$  electronic origin. See text for explanation. The  $T_{1g} + \nu_4$  transition is broadened by interaction with the host  $\nu_4$ .

Figure 8

Four moderately intense features of ( $A_{1g} + T_{1g}$ )  $\leftarrow E_g$  transition shown at  $4.2^\circ\text{K}$  for a 1%  $\text{OsF}_6/\text{MoF}_6$  sample. These are assigned as components of  $\nu_5$  which is perturbed by a  $T_{1g} \times t_2$  LJTE with  $D = 2.2$ . See text for discussion.

Figure 9

The stretching region of the  $4,000\text{ cm}^{-1}$  ( $A_{1g} + T_{1g}$ )  $\leftarrow E_g$  transition at  $4.2^\circ\text{K}$  for a 1%  $\text{OsF}_6/\text{MoF}_6$  sample. Note that most of the transitions assignable are features built on the  $A_{1g}$  origin. Assignments of  $\nu_2/\nu_3$  built on the  $T_{1g}$  origin are made by default.

Figure 10

Four proposed models explaining hot band structure of  $4,000\text{ cm}^{-1}$   $A_{1g} \leftarrow (E_g + T_{2g})$  absorption transition. The arrows represent absorption transitions from the ground ( $E_g + T_{2g}$ ) states to the  $A_{1g}$  origin. Both the  $E_g$  and  $T_{2g}$  states are assumed split by the low symmetry crystal field. Boltzman factors (relative populations) are given for each level at  $77^\circ\text{K}$ . Model(a) is the only model not ruled out by intensity patterns.

Figure 11

A survey absorption spectrum of the  $8,000\text{ cm}^{-1}$  ( $E_g + T_{2g}$ )  $\leftarrow E_g$  transition. This system evidences none of the usual hexafluoride vibronic patterns, presumably due to vibronic coupling. The origin transition, false origins, and  $\nu_1$  are indicated.

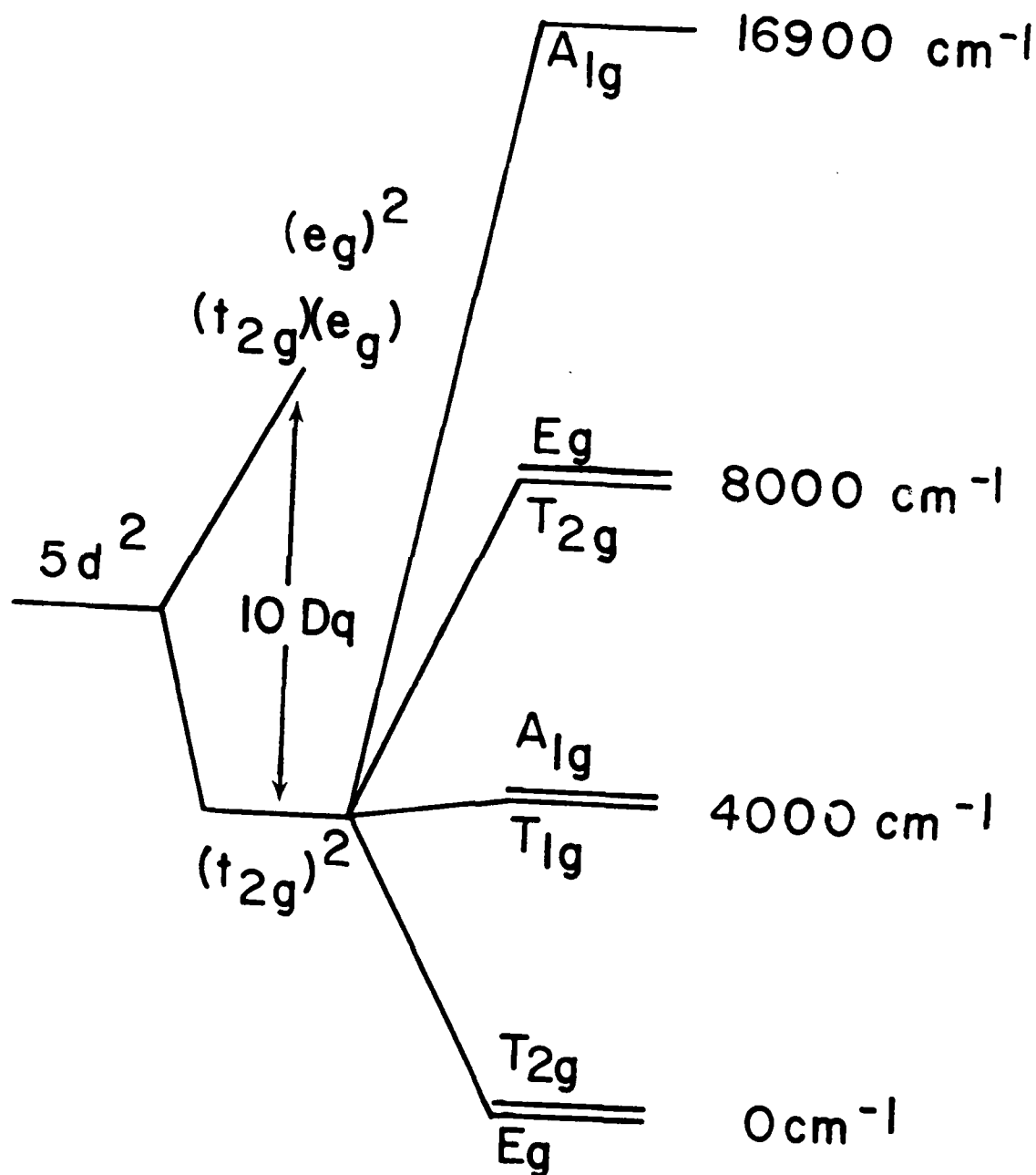
Figure 12

A survey Raman spectrum of  $4,000\text{ cm}^{-1}$  ( $A_{1g} + T_{1g}$ ) at  $77^\circ\text{K}$  for a 5%  $\text{OsF}_6/\text{MoF}_6$  sample. Intensities are 1000 cps for the origin, 30 cps for  $\nu_5$ , and 100 cps for  $\nu_1$ .

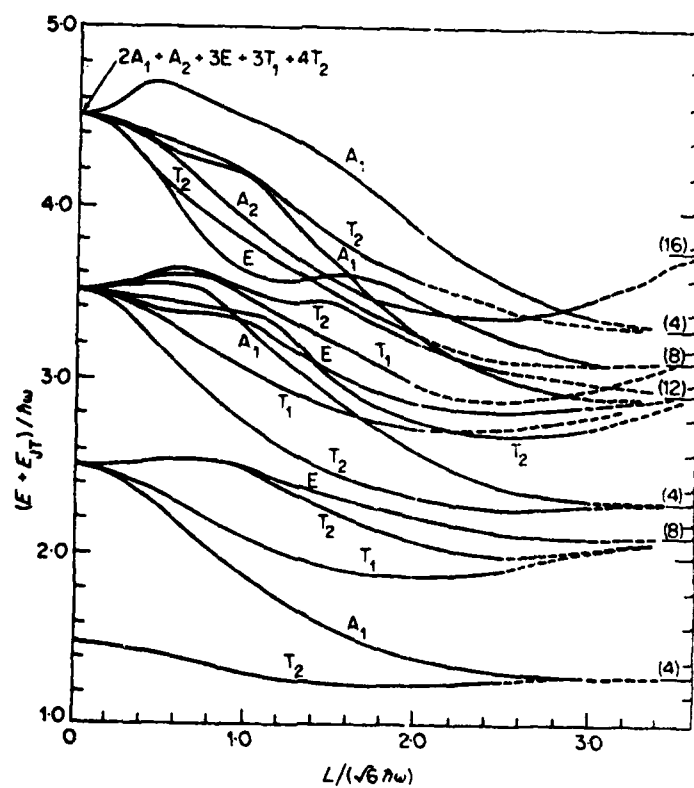
Figure 13

High resolution spectrum of  $4,000\text{ cm}^{-1}$  ( $A_{1g} + T_{1g}$ ) origin region at  $77^\circ\text{K}$  for a 5%  $\text{OsF}_6/\text{MoF}_6$  sample. The highest energy feature is the  $A_{1g}$  origin. The other three features are hot bands.

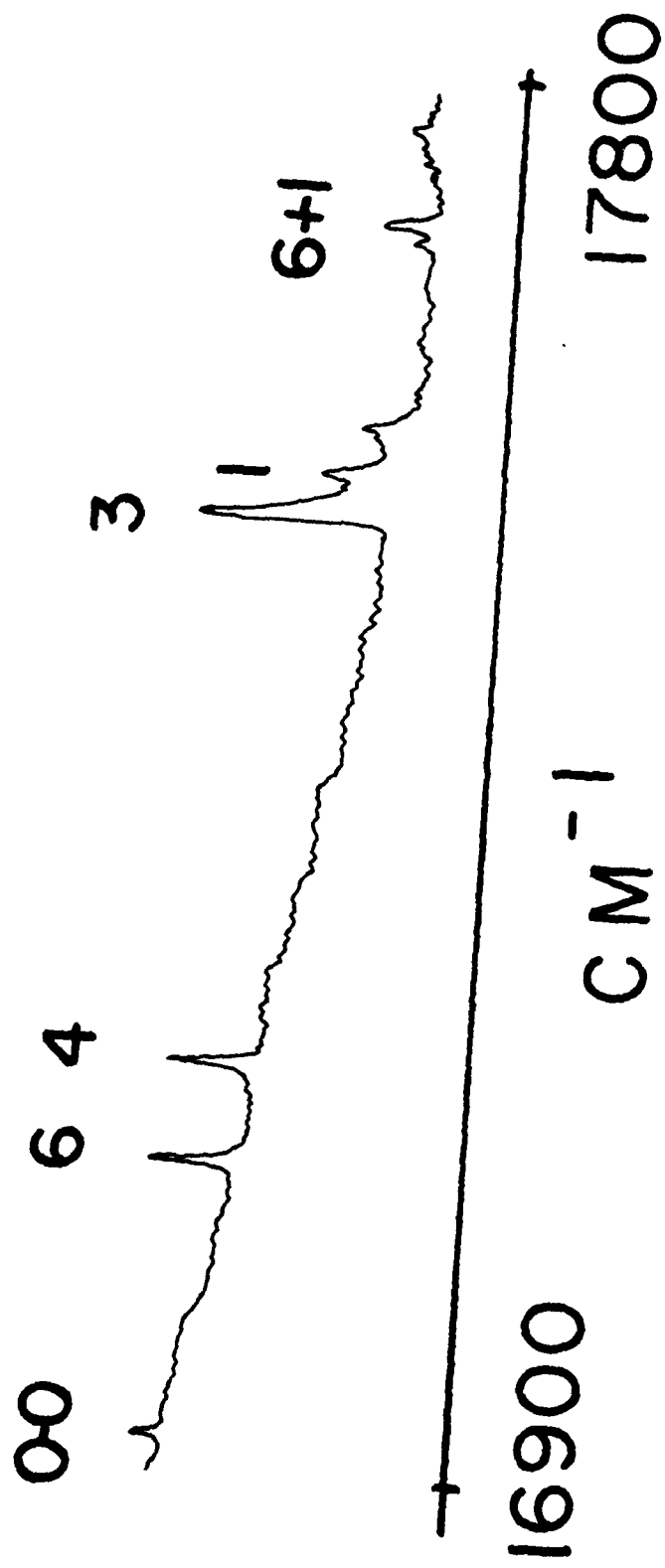
# $\text{OsF}_6$ Energy Levels



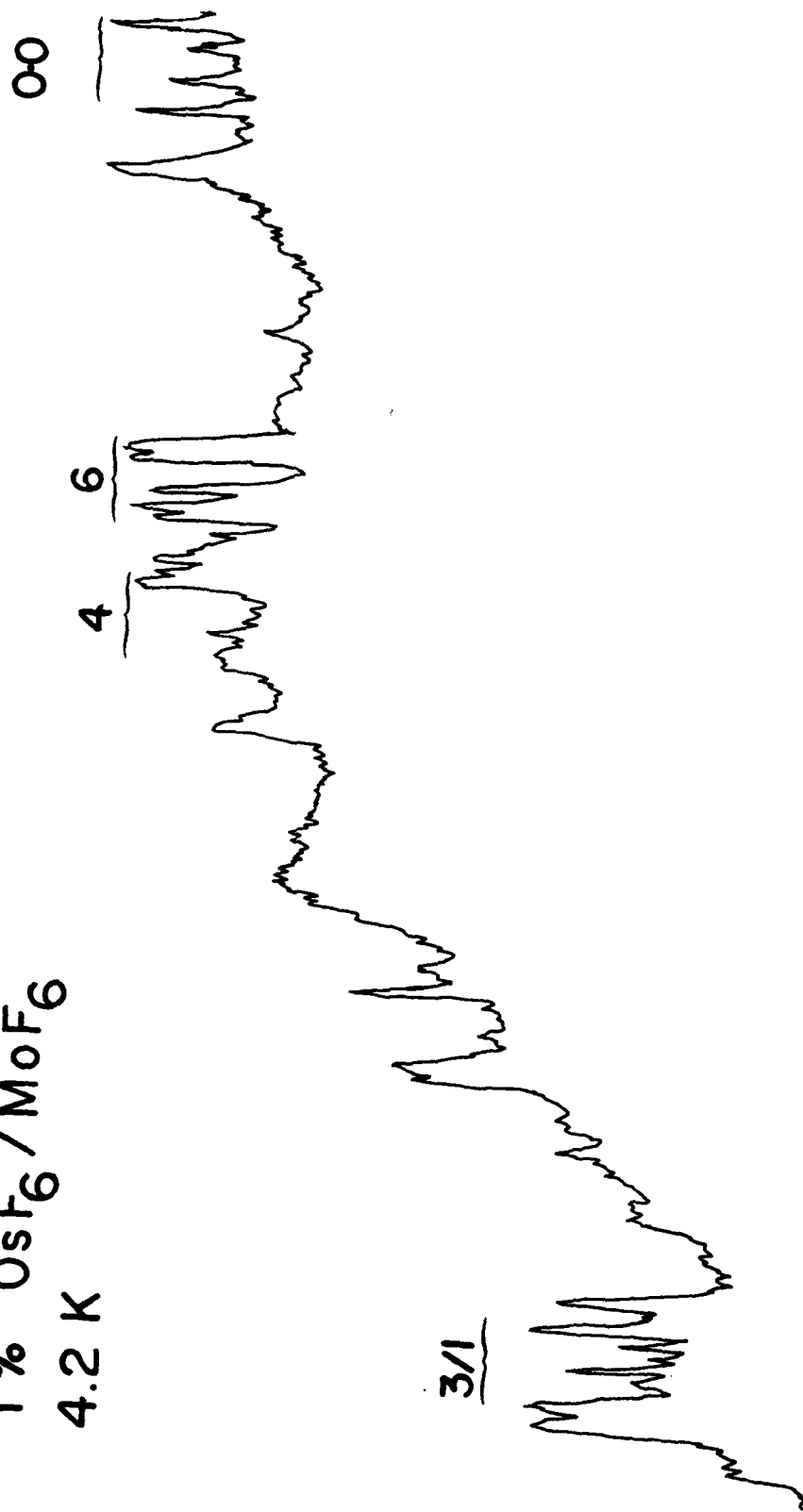
$$H_O + H_{cf} + (H_{so} + H_c)$$



1% OsF<sub>6</sub> / MoF<sub>6</sub>  
4°K



1%  $\text{OsF}_6 / \text{MoF}_6$   
4.2 K

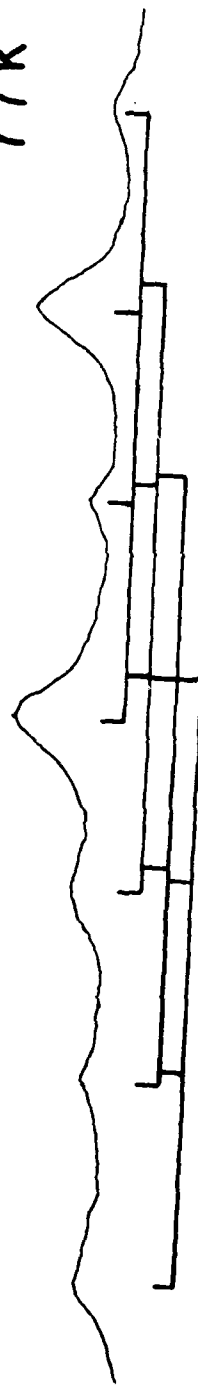


1%  $\text{OsF}_6$  /  $\text{MoF}_6$



4.2 K

77 K



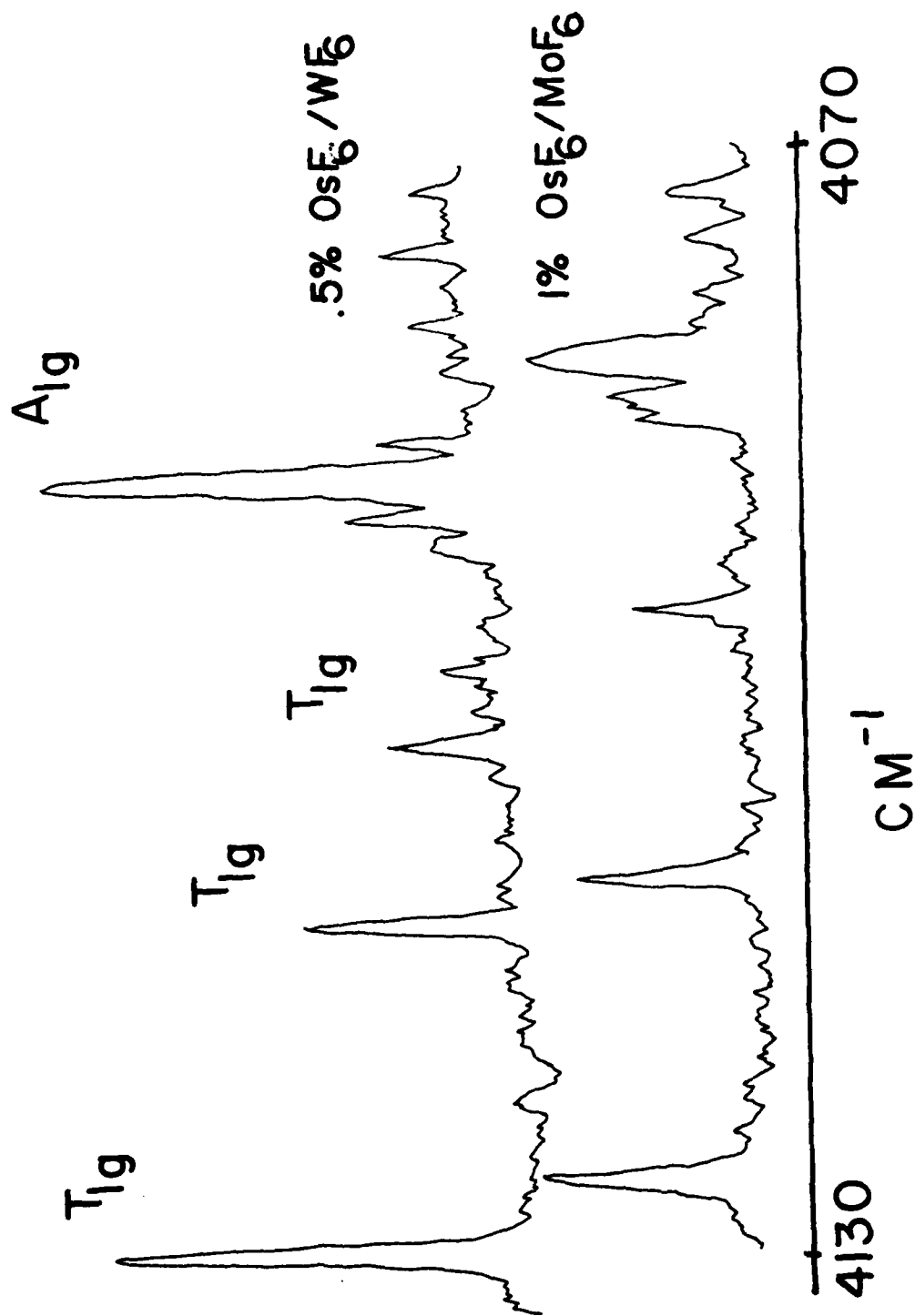
4130

$\text{CM}^{-1}$

4040

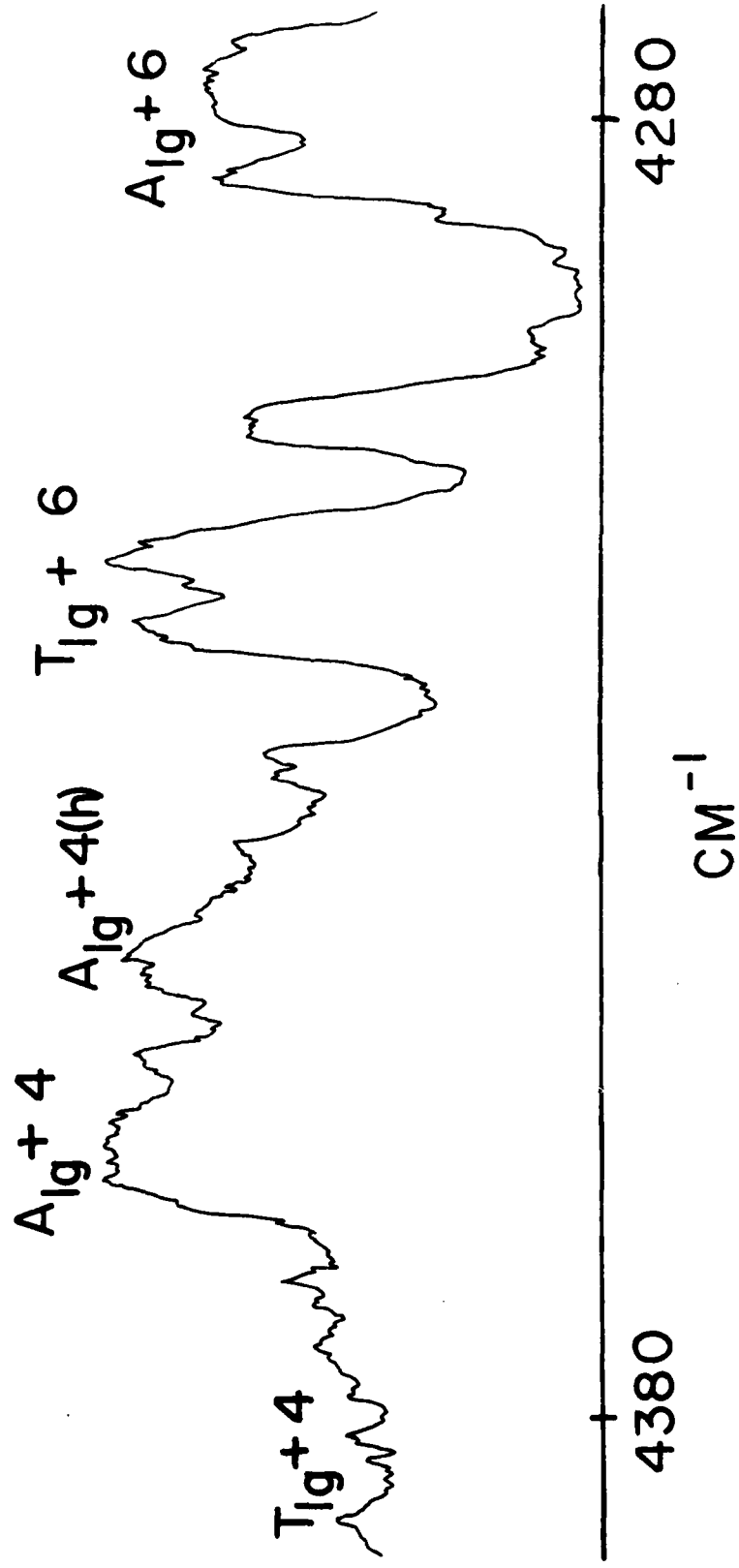


4.2 K



1% OsF<sub>6</sub>/MoF<sub>6</sub>

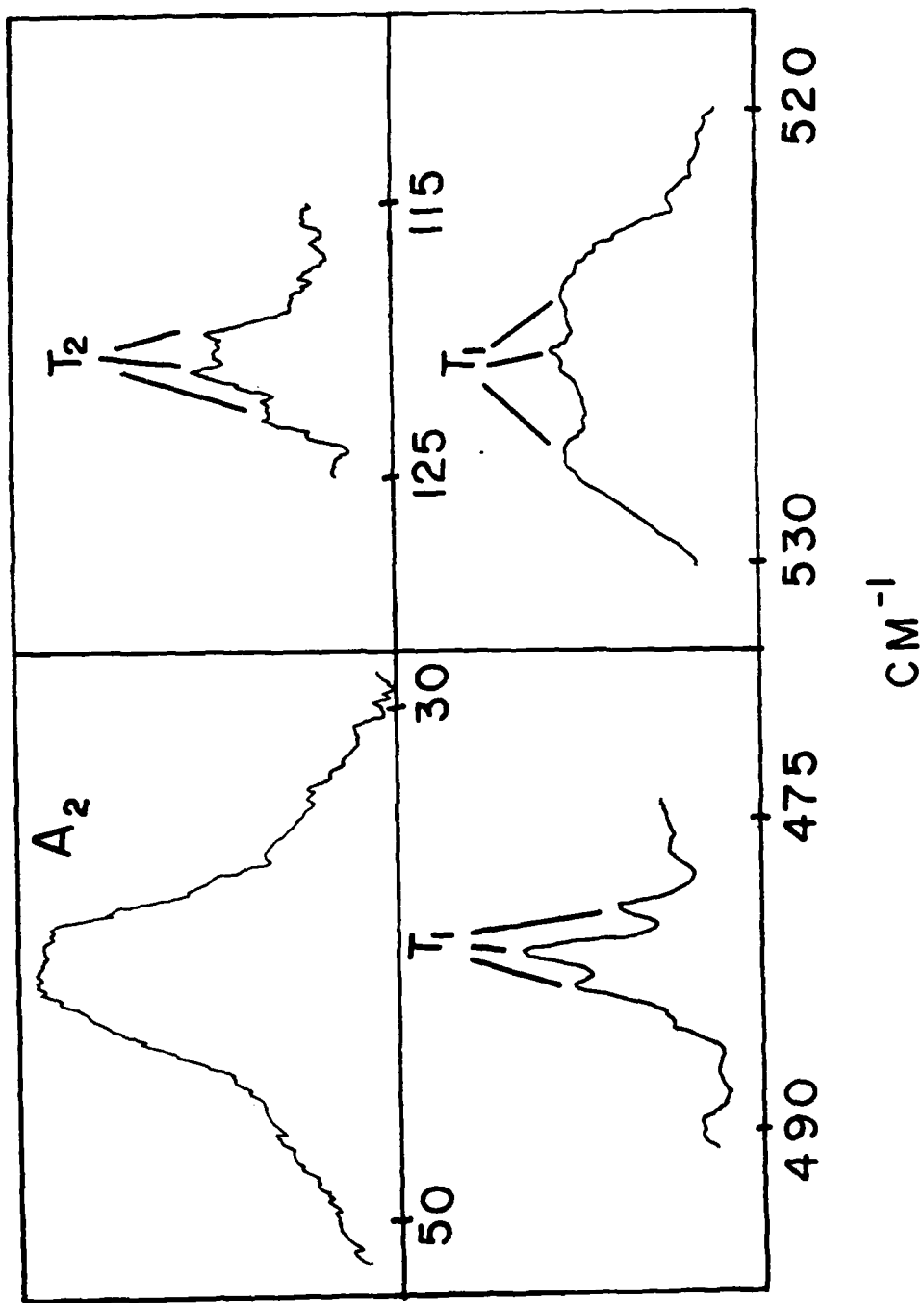
4.2 K



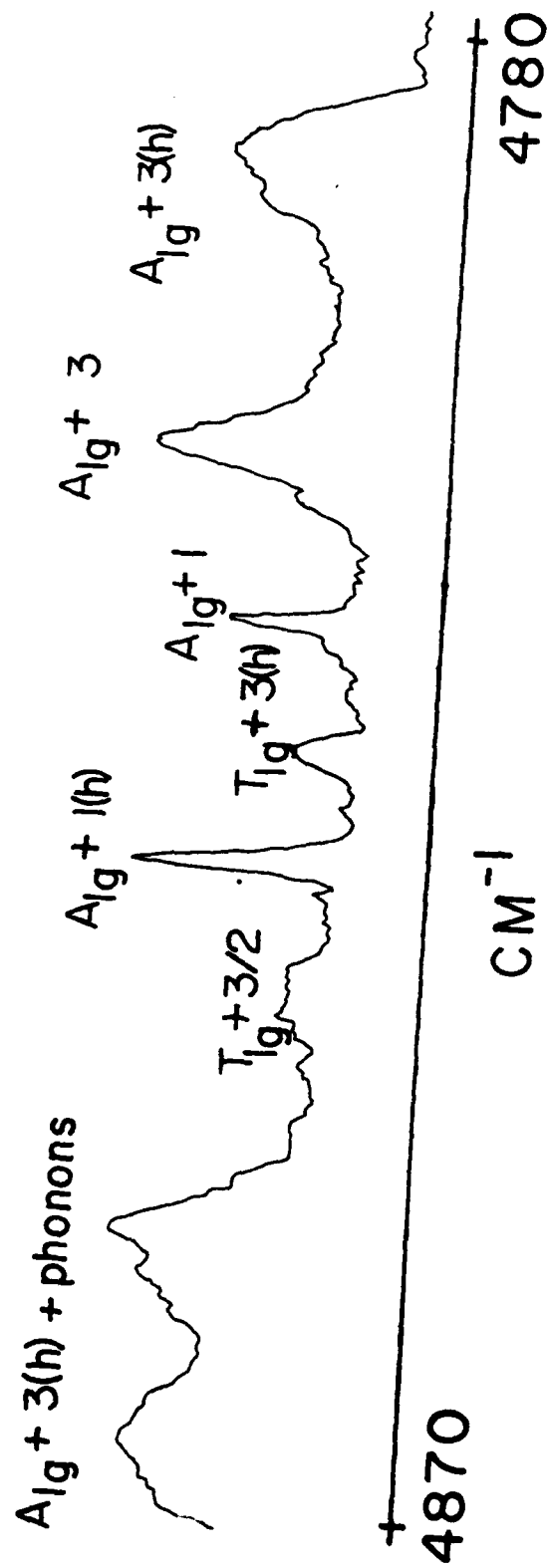
1% OsF<sub>6</sub> / MoF<sub>6</sub>

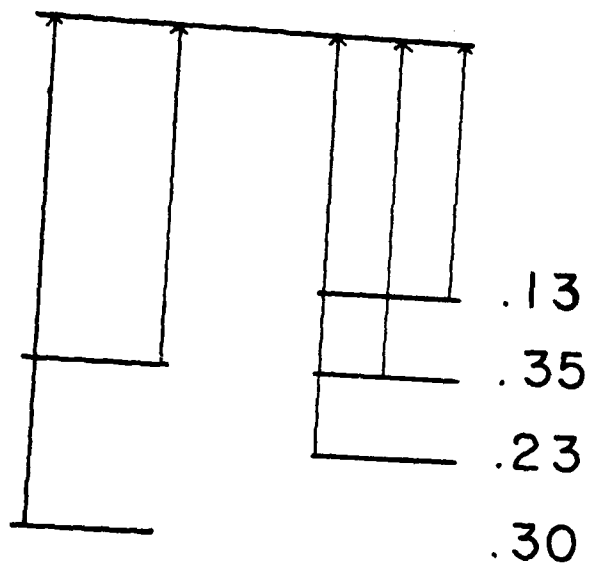
4.2°K

T<sub>1g</sub> + ν<sub>5</sub>

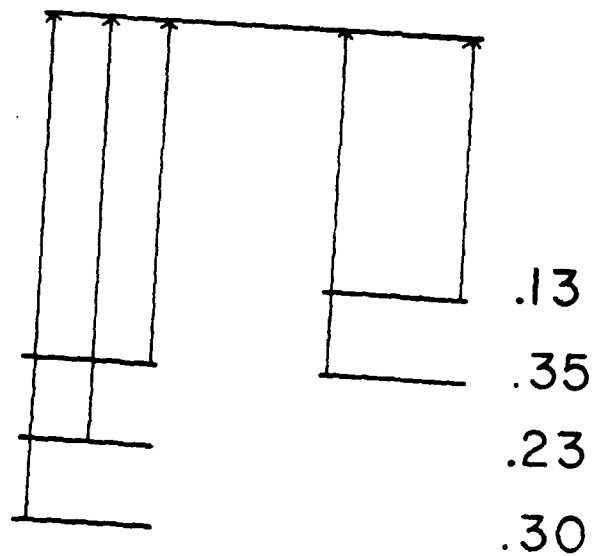


1%  $\text{OsF}_6/\text{MoF}_6$   
4.2 K

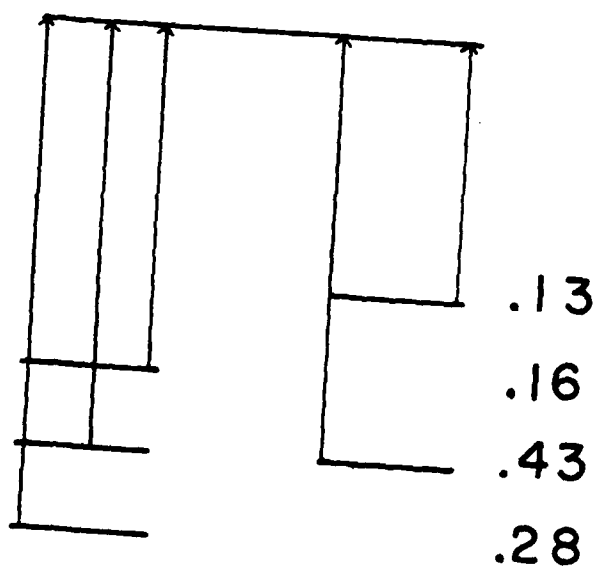




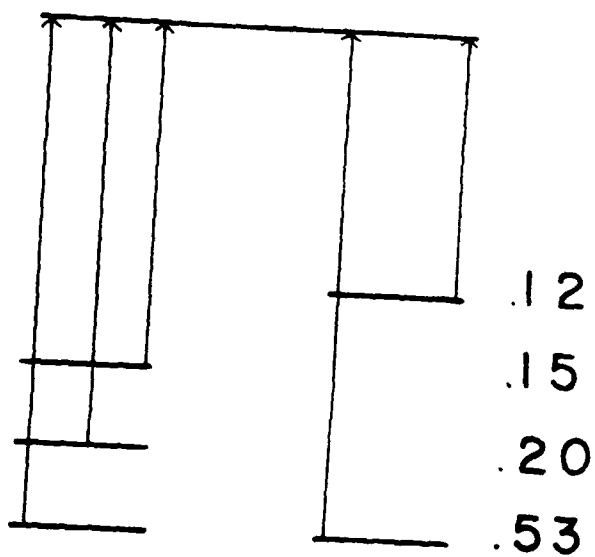
(a)



(b)

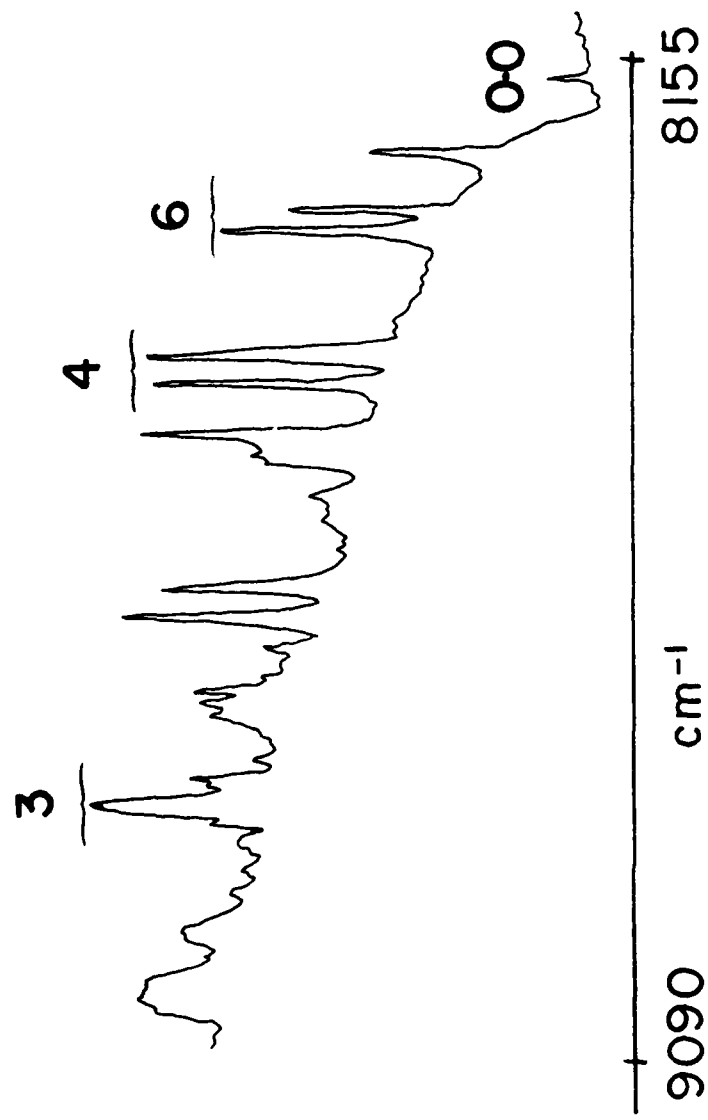


(c)



(d)

1% OsF<sub>6</sub>/MoF<sub>6</sub>  
4°K



5% OsF<sub>6</sub> / MoF<sub>6</sub>

77 K

0-0

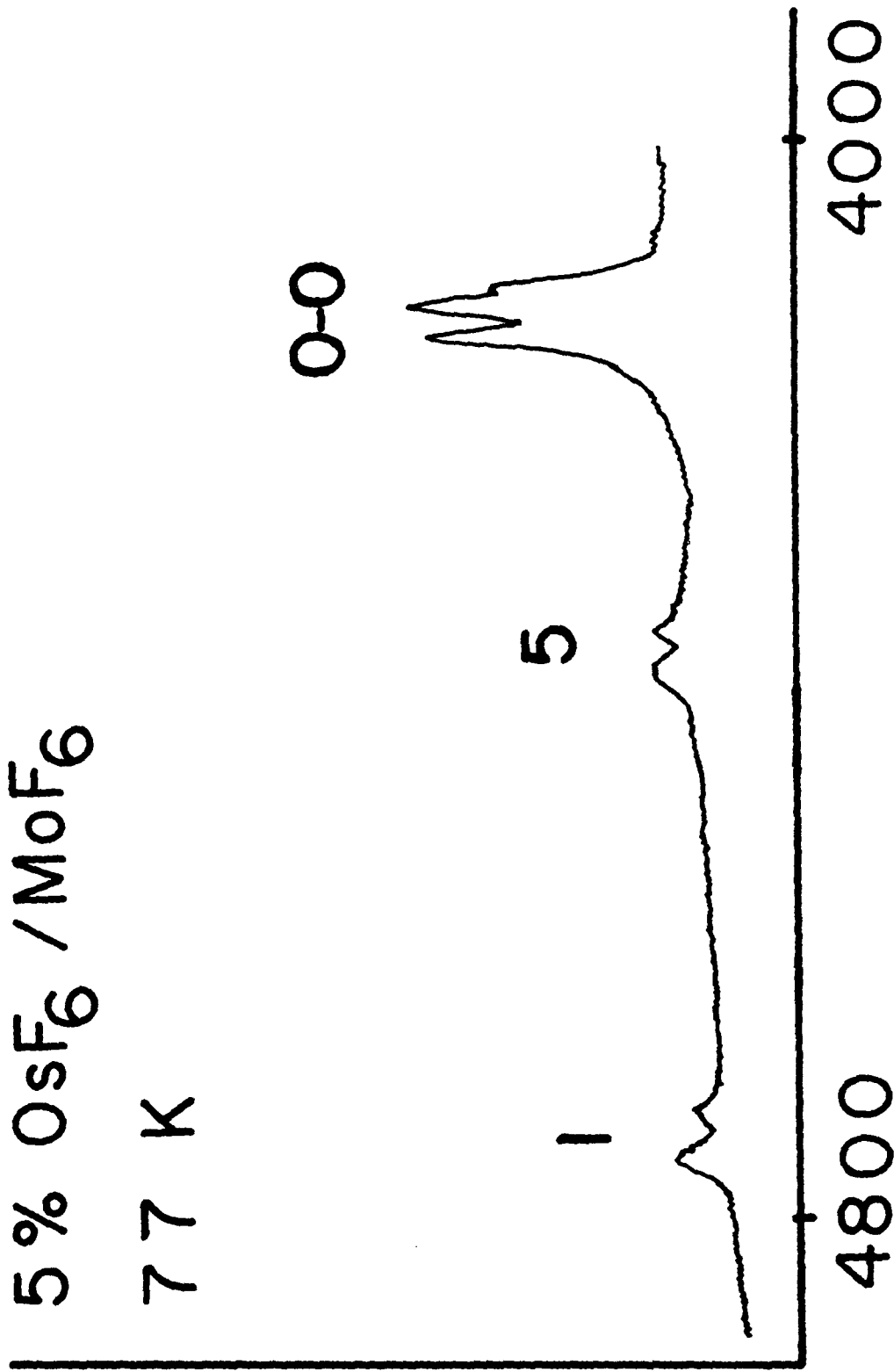
5

1

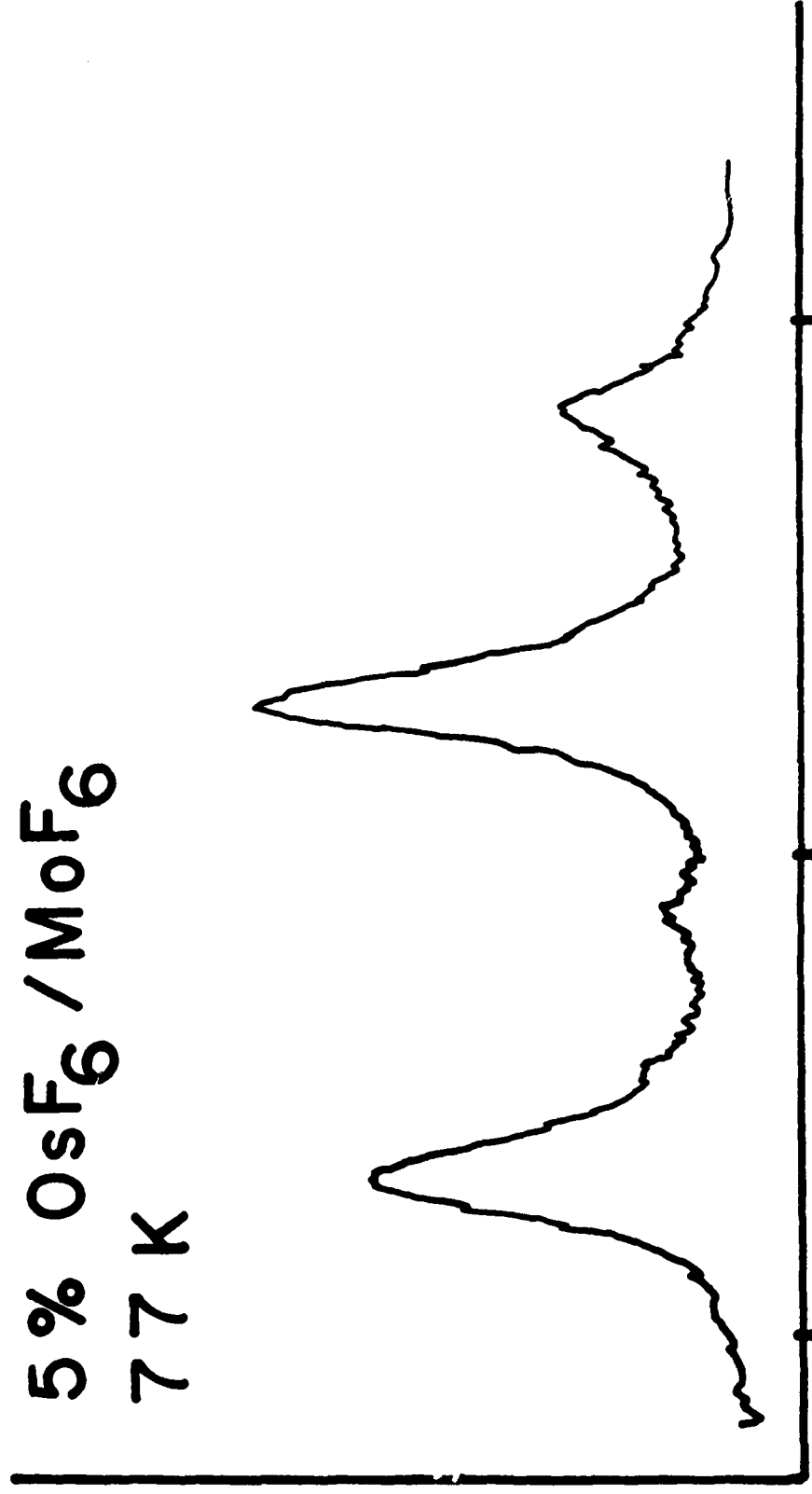
4800

4000

Stokes Shift (cm<sup>-1</sup>)



5% OsF<sub>6</sub> / MoF<sub>6</sub>  
77 K



4025

4110

Stokes Shift (cm<sup>-1</sup>)



TECHNICAL REPORT DISTRIBUTION LIST, 051A

	<u>No. Copies</u>		<u>No. Copies</u>
Dr. M. A. El-Sayed Department of Chemistry University of California, Los Angeles Los Angeles, California 90024	1	Dr. M. Rauhut Chemical Research Division American Cyanamid Company Bound Brook, New Jersey 08805	1
		Dr. J. I. Zink Department of Chemistry University of California, Los Angeles Los Angeles, California 90024	1
Dr. C. A. Heller Naval Weapons Center Code 6059 China Lake, California 93555	1	Dr. D. Haarer IBM San Jose Research Center 5600 Cottle Road San Jose, California 95143	1
Dr. J. R. MacDonald Chemistry Division Naval Research Laboratory Code 6110 Washington, D.C. 20375	1	Dr. John Cooper Code 6130 Naval Research Laboratory Washington, D.C. 20375	1
Dr. G. B. Schuster Chemistry Department University of Illinois Urbana, Illinois 61801	1	Dr. William M. Jackson Department of Chemistry Howard University Washington, DC 20059	1
Dr. A. Adamson Department of Chemistry University of Southern California Los Angeles, California 90007	1	Dr. George E. Walraffen Department of Chemistry Howard University Washington, DC 20059	1
Dr. M. S. Wrighton Department of Chemistry Massachusetts Institute of Technology Cambridge, Massachusetts 02139	1		

TECHNICAL REPORT DISTRIBUTION LIST, GEN

	<u>No.</u> <u>Copies</u>
Mr. James Kelley DTNSRDC Code 2803 Annapolis, Maryland 21402	1
Mr. A. M. Anzalone Administrative Librarian PLASTEC/ARRADCOM Bldg 3401 Dover, New Jersey 07801	1

TECHNICAL REPORT DISTRIBUTION LIST, GEN

	<u>No.</u> <u>Copies</u>		<u>No.</u> <u>Copies</u>
Office of Naval Research Attn: Code 472 800 North Quincy Street Arlington, Virginia 22217	2	U.S. Army Research Office Attn: CRD-AA-IP P.O. Box 1211 Research Triangle Park, N.C. 27709	1
ONR Western Regional Office Attn: Dr. R. J. Marcus 1030 East Green Street Pasadena, California 91106	1	Naval Ocean Systems Center Attn: Mr. Joe McCartney San Diego, California 92152	1
ONR Eastern Regional Office Attn: Dr. L. H. Peebles Building 114, Section D 666 Summer Street Boston, Massachusetts 02210	1	Naval Weapons Center Attn: Dr. A. B. Amster, Chemistry Division China Lake, California 93555	1
Director, Naval Research Laboratory Attn: Code 6100 Washington, D.C. 20390	1	Naval Civil Engineering Laboratory Attn: Dr. R. W. Drisko Port Hueneme, California 93401	1
The Assistant Secretary of the Navy (RE&S) Department of the Navy Room 4E736, Pentagon Washington, D.C. 20350	1	Department of Physics & Chemistry Naval Postgraduate School Monterey, California 93940	1
Commander, Naval Air Systems Command Attn: Code 310C (H. Rosenwasser) Department of the Navy Washington, D.C. 20360	1	Scientific Advisor Commandant of the Marine Corps (Code RD-1) Washington, D.C. 20380	1
Defense Technical Information Center Building 5, Cameron Station Alexandria, Virginia 22314	12	Naval Ship Research and Development Center Attn: Dr. G. Bosmajian, Applied Chemistry Division Annapolis, Maryland 21401	1
Dr. Fred Saalfeld Chemistry Division, Code 6100 Naval Research Laboratory Washington, D.C. 20375	1	Naval Ocean Systems Center Attn: Dr. S. Yamamoto, Marine Sciences Division San Diego, California 91232	1
		Mr. John Boyle Materials Branch Naval Ship Engineering Center Philadelphia, Pennsylvania 19112	1

**DAT**  
**ILMI**